JOURNAL OF

ALLOYS AND COMPOUNDS

An interdisciplinary journal with focus on Solid State Chemistry and Physics

materialstoday

ScienceDirect

Journal of Alloys and Compounds

Supports *open access*

7.6 CiteScore

4.65 Impact Factor

Menu

Search in this journal

Submit your article

Guide for authors

About the journal

Aims and scope | Editorial board | Abstracting and indexing

Editor-in-Chief

Senior Editors

Daria Drozdenko
Charles University Faculty of Mathematics and Physics Department of Physics of Materials, 3 Ke Karlovu, 121 16, Praha, Czech Republic
Analysis of plastic deformation in metals by acoustic emission (AE) technique., Complex study of Mg alloys (including Mg-LPSO-based alloys), microstructure and mechanical properties, Advanced techniques for microstructure analysis

Dmitry G. Eskin
Brunel University Brunel Centre for Advanced Solidification Technology, UB8 3PH, Uxbridge, United Kingdom
structure refinement, degassing, exfoliation, metal processing, solidification

Huiqing Fan
Northwestern Polytechnical University School of Materials Science and Engineering, 127 Youyixilu, 710072, Xian, China
Functional Ceramics, Nano Materials, Thin Films

Josef Fidler
TU Wien Institute of Solid State Physics, Wiedner Hauptstrasse 8-10, 1040, Wien, Austria

Thiagarajan Gnanasekaran
Indira Gandhi Centre for Atomic Research, Indira Gandhi Centre for Atomic Research,Kalpakkam, 603102, Kalpakkam, India
Phase Diagrams; Measurement of Thermochemical Properties; Solid State Ionics; Chemical Sensors and Sensor Materials; Hydrogen in Metals; Chemical Synthesis of Inorganic Compounds

Mohamed Henini
University of Nottingham School of Physics and Astronomy, University Park, NG7 2RD, Nottingham, United Kingdom
Low Dimensional Structures and Devices, Nanotechnoloy and Nanoscience, Self-Assembled Semiconductor Nanostructures, Semiconductor Materials, III-V Electronic and Optoelectronic Devices, Photovoltaic Materials and Devices, Molecular Beam Epitaxy, Deep Level Transient Spectroscopy

Jacques Huot
University of Quebec in Trois Rivieres Hydrogen Research Institute, 3351 Boulevard Des Forges (P.O. Box 500), Trois Rivieres, G9A 5H7, Quebec, Canada
Hydrogen research, Hydrogen storage, Metal hydrides, Gas-solid interactions, Materials characterization, Neutron diffraction, Materials synthesis

Li Jin
Shanghai Jiao Tong University School of Materials Science and Engineering, 1954 Hua Shan Road, 2000030, Shanghai, China
Texture of Mg alloys, Texture induced deformation behaviour, Metal forming, Application of light alloys

Yongchang Liu
Tianjin University, 300072, Tianjin, China

Solid-state phase transformations: thermodynamic and kinetic analyses; rapid solidification; metal-activated sintering and Microstructural control in ni(co)-based superalloys, heat-resistance steels, superconducting materials, lead-free solders and ti-al intermetallic compounds.

Nicoleta Lupu
National Institute of Research and Development for Technical Physics, Mangeron Av 47, 6600, Iaşi, Romania
Metallic glasses; Bulk metallic glasses; Magnetic and magnetoelectric materials; Magnetoelastic processes; sensors and devices; Physics and chemistry of surfaces and interfaces; Nanoparticles and nanowire arrays; Hydrogen storage materials.

Valmor Mastelaro
University of Sao Paulo Campus of Sao Carlos, Sao Carlos, Brazil
Structure-property relationships, ZnO Based Materials, Metal Oxide Gas sensors, Glass and Glass-Ceramics, Metal oxide thin films, XAS and XPS spectroscopies

BS Murty
Indian Institute of Technology Hyderabad, IITH Main Road, Near NH-65, Sangareddy, 502285, Kandi, India
Physical metallurgy, alloy design, Phase transformations, High entropy alloys, bulk metallic glasses, nanocrystalline materials, metal matrix composites, electron microscopy, atom probe tomography.

Hari Srikanth
University of South Florida Department of Physics, 4202 E Fowler Ave, Tampa, Florida, FL 33620, United States
Magnetism and magnetic materials, Nanostructured materials for energy and biomedical applications, Structure-property correlations in functional materials, Strongly correlated systems

Wieslaw Strek
Institute of Low Temperature and Structure Research Polish Academy of Sciences, Okólna str. 2, 50-422, Wroclaw, Poland
Rare earth ions and transition metal ions, doped sol-gel materials, photonic structures, nanomaterials, nanoceramics and crystals.

Isabel Van Driessche
Ghent University Department of Chemistry, Krijgslaan 281 (Building S3), 9000, Gent, Belgium
Chemical Solution deposition (CSD, ink jet printing) of ceramics. Materials of interest : superconducting perovskites and buffer layers for production of coated conductors, titanates for (photo)catalytic and battery applications, low-E coatings; Formulation of environmentally friendly based inks. Use of bottom-up chemical synthesis approaches (hydrothermal, microwave-assisted, hot injection) for the synthesis of ceramic nanoparticles/suspensions.

Mingzhong Wu
Colorado State University Department of Physics, 1875 Campus Delivery, Fort Collins, Colorado, CO 80523, United States
Experimental Condensed Matter: Magnetism, Magnetic Materials, Spintronics, and Spin Caloritronics

Renbing Wu
Fudan University Department of Material Science, 200433, Shanghai, China
Semiconductor, Transition Metal-based composites, Electrode materials for energy storage and conversion

Xuezhang Xiao
Zhejiang University School of Materials Science and Engineering, 38 Zheda Road, Hangzhou, China

Volodymyr Yartys
Institute for Energy Technology, 2027, Kjeller, Norway
Nanomaterials for energy storage. Rechargeable Batteries. Hydrogen as an Energy Carrier. New Intermetallics and Carbon Materials for Hydrogen Storage and Battery Applications. Synchrotron and neutron powder diffraction. Crystal structures of novel materials.

Editorial Advisory Board

G. Adachi
Osaka, Japan
Chemistry and materials science of rare earths, Solid state electrochemistry

A.V. Andreev
Praha, Czech Republic
Magnetism of rare-earth and uranium intermetallics, Crystal structure of rare-earth and uranium intermetallics, Metallic hydrides, Permanent magnets

A. Dahle
Jonkoping, Sweden
Solidification, Rheology, Light alloys, Lead-free soldering, Hydrogen storage

F.J. Di Salvo
Ithaca, New York, United States
Synthesis and characterization of solid state compounds, novel crystal structures. Physical properties such as electrical resistivity, thermal conductivity, thermopower.

T.B. Flanagan
Burlington, Vermont, United States
Hydrogen diffusion through metals and alloys, Thermodynamics of H metal systems, Characterization of intermetallic-H systems

C. Gomez Polo
Pamplona, Spain
Magnetism; magnetic nanoparticles and nanostructured magnetic materials; transition metal oxides

J.-M. Greneche
Le Mans, France

V.G. Harris
Boston, Massachusetts, United States
Magnetoceramics, principally ferrites, rf materials, magnetism

Hsiang Hsing-I, PhD
National Cheng Kung University College of Engineering, Tainan, Taiwan
Ceramic processing, Electroceramics, CIGS/CZTS, Powder synthesis

D.C. Johnson
Eugene, Oregon, United States
Solid state chemistry, Thermoelectric materials, X-ray reflectivity, Thermal conductivity, Electrical transport

H. Kleinke
Waterloo, Ontario, Canada
Solid state chemistry, materials chemistry, energy conversion, thermoelectric materials, transport properties, electronic structure calculations, crystal structures, chalcogenides, pnictides

E.J. Mittermeijer
Stuttgart, Germany
Phase transformations, (interface) thermodynamics and kinetics; Nanomaterials, their unusual properties; Stress and phase transformations in (very) thin (multi)layers; surface engineering (nitriding and nitrocarburizing of iron, iron alloys and steels); oxidation of metals and alloys

Y. Mozharivskyj
Hamilton, Ontario, Canada
Thermoelectric materials, Magnetocaloric materials, X-ray analysis

R. Nesper
Zurich, Switzerland
Inorganic chemistry, Zintl phases, nanoscience, intermetallic phases, electrochemistry, hard materials.

E. Peterson
Los Alamos, New Mexico, United States
Actinide thermodynamics and equilibrium phase diagrams, High temperature superconductor synthesis, characterization, and applications, Carbon nanotubes, Radiation damage, and Vaporization studies

W. Prellier
Caen, France

K. Z. Rožman
Ljubljana, Slovenia

H. Sakaguchi
Tottori, Japan
Li ion materials, Hydrogen storage materials, hydrides

H. Sato
Tokyo, Japan

O.N. Senkov
Dayton, Ohio, United States

K. Suzuki
Miyagi, Japan

T. Takabatake
Higashihiroshima, Japan

T. Yamase
Yokohama, Japan
Catalysis, photoluminescence.

C.-L. Yeh
Taichung, Taiwan
Self-propagating High-temperature Synthesis (SHS), Transition metal borides and nitrides, Intermetallics, MAX phases, Thermite Reaction

All members of the Editorial Board have identified their affiliated institutions or organizations, along with the corresponding country or geographic region. Elsevier remains neutral with regard to any jurisdictional claims.

ISSN: 0925-8388

Journal of Alloys and Compounds

Supports *open access*

Volume 860

15 April 2021

Previous vol/issue

Next vol/issue

Full text access

Editorial Board

Article 158694

Download PDF

Research article ○ Abstract only

Optimized synergistic preparation of nitrogen-doped porous carbon derived from gasified carbon for supercapacitors

Yang Cao, Kuihua Han, Zhaocai Teng, Jinxiao Li, ... Jigang Zhang

Article 158385

Purchase PDF Article preview

Research article ○ Abstract only

Enhanced age hardening response and precipitation evolution of elastic stress aged Mg–Zn alloys

Yongjian Wang, Liping Zhong, Yuchen Dou, Zhenyi Huang

Article 158513

Purchase PDF Article preview

Research article ○ Abstract only

Thermally-enhanced microstructures of Si/TiNi film electrodes for improved electrochemical properties

Gyu-Bong Cho, Jin-Hoon Ju, Won-Tae Lee, Sang-Hee Park, ... Tae-Hyun Nam

Article 158507

Journal of Alloys and Compounds
Supports *open access*

Menu

7.6 CiteScore
4. In

Article 158436

Purchase PDF Article preview

Research article ○ Abstract only

Microstructures and mechanical properties of $CrFeNi_2Nb_x$ eutectic multicomponent alloys

Won-hyuk Lee, Yeonju Oh, Min-Gu Jo, Heung Nam Han, Yanghoo Kim

Article 158502

Purchase PDF Article preview

Research article ○ Abstract only

Mechanical properties of rolled and aged AA6061 sheets at room-temperature and cryogenic environments

Yue Liu, Xiangshuai Zhao, Jing Li, Laxman Bhatta, ... Hailiang Yu

Article 158449

Purchase PDF Article preview

Research article ○ Abstract only

Scalable synthesis of highly luminescent and stable thiocyanate based $CsPbX_3$ perovskite nanocrystals for efficient white light-emitting diodes

Saroj Thapa, Gopi Chandra Adhikari, Hongyang Zhu, Peifen Zhu

Article 158501

Purchase PDF Article preview

Research article ○ Abstract only

Comparative investigation on the functional properties of alkaline earth metal (Ca, Ba, Sr) doped $Nd_2NiO_{4+\delta}$ oxygen electrode material for SOFC applications

R.K. Lenka, P.K. Patro, Vivek Patel, L. Muhmood, T. Mahata

Article 158490

Purchase PDF Article preview

Research article ○ Abstract only

Hydration effect on properties of the $La_{2-x}A_xNi_{1-y}Fe_yO_{4+\delta}$ (A=Ca, Sr) cathode materials for H^+-SOFCs

A.R. Gilev, E.A. Kiselev, D.A. Malyshkin, K.S. Sukhanov, V.A. Cherepanov

Article 158452

Purchase PDF Article preview

Research article ○ Abstract only

Preparation of RF sputtered AZO/Cu/AZO multilayer films and the investigation of Cu thickness and substrate effects on their microstructural and optoelectronic properties

Djelloul Mendil, Fatiha Challali, Tahar Touam, Valérie Bockelée, ... Azeddine Chelouche

Article 158470

Purchase PDF Article preview

Journal of Alloys and Compounds
Supports *open access*

Menu

7.6 CiteScore
4. In

Research article ○ Abstract only
Nanorods-assembled ZnO microflower as a powerful channel for n-butanol sensing
Wei Yang, Xiao Xiao, Baijun Fang, Hexia Deng
Article 158410
Purchase PDF Article preview

Research article ○ Abstract only
Growth and electrical properties of n-type monolayer sulfur-doped graphene film in air
Pingjian Li, Kesai Xu, Yu Zhou, Yuanfu Chen, ... Xuesong Li
Article 158462
Purchase PDF Article preview

Research article ○ Abstract only
Fabrication of in-situ grown and Pt-decorated ZnO nanoclusters on new-type FTO electrode for room-temperature detection of low-concentration H_2S
Jingyue Xuan, Guodong Zhao, Qianqian Gong, Lili Wang, ... Bo Liu
Article 158499
Purchase PDF Article preview

Review article ○ Abstract only
Recent advances in development of magnetic garnet thin films for applications in spintronics and photonics
Yucong Yang, Tao Liu, Lei Bi, Longjiang Deng
Article 158235
Purchase PDF Article preview

Research article ○ Abstract only
Mechanical properties and microstructural evolution of a novel $(FeCoNi)_{86.93}Al_{6.17}Ti_{6.9}$ medium entropy alloy fabricated via powder metallurgy technique
Ao Fu, Bin Liu, Shenghang Xu, Jing Huang, ... Yong Liu
Article 158460
Purchase PDF Article preview

Research article ○ Abstract only
Microstructure and arc erosion behaviors of Ag-CuO contact material prepared by selective laser melting
Siyu Chen, Jun Wang, Zhao Yuan, Zhe Wang, Dan Du
Article 158494
Purchase PDF Article preview

Research article ○ Abstract only
Yb^{3+}/Tm^{3+} and Yb^{3+}/Ho^{3+} doped $NaY_9(SiO_4)_6O_2$ phosphors: Upconversion luminescence processes, temperature-dependent emission spectra and optical temperature-sensing properties

Journal of Alloys and Compounds
Supports *open access*

Menu

7.6 CiteScore
4. In

Understanding the improvement of fluorination in 5.3 V $LiCoMnO_4$ spinel
Sanchao Liu, Huihui He, Chengkang Chang
Article 158468

Purchase PDF Article preview

Research article ○ Abstract only
The existence and origin of field-induced ferrimagnetic order transition of $LuFe_2O_4$ single crystal
Feng Yang, Qiyuan Feng, Zhengcai Xia, Qingyou Lu, ... Zhaoming Tian
Article 158426

Purchase PDF Article preview

Research article ○ Abstract only
New criteria for the applicability of combustion synthesis: The investigation of thermodynamic and kinetic processes for binary Chemical Reactions
Xiaoming Tan, Xianli Su, Yonggao Yan, Ctirad Uher, ... Xinfeng Tang
Article 158465

Purchase PDF Article preview

Research article ○ Abstract only
High shock resistance and self-healing ability of graphene/nanotwinned Cu nanolayered composites
Che Zhang, Ajit Godbole, Guillaume Michal, Cheng Lu
Article 158435

Purchase PDF Article preview

Research article ○ Abstract only
Porous hollow $ZnCo_2S_4$ nanosheet arrays derived from metal-organic framework as efficient cathode for lithium oxygen batteries
Peng Zhang, Xiaobin Hui, Huiyang Wang, Xueping Gao, Longwei Yin
Article 157656

Purchase PDF Article preview

Research article ○ Abstract only
Bismuth oxycarbonate Nanoplates@α-$Ni(OH)_2$ nanosheets 2D plate-on-sheet heterostructure as electrode for high-performance supercapacitor
Manjunath Shetty, Karnan Manickavasakam, Nagendra Kulal, Prasanna D. Shivaramu, ... Dinesh Rangappa
Article 158495

Purchase PDF Article preview

Research article ○ Abstract only
Flexible asymmetric supercapacitors based on $NiCo_2O_4$ in a neutral electrolyte achieving 2.4 V voltage window
Shiqian Chen, Ping Gao, Dongwei Zhang, Lilin Lin, ... Jinwei Gao
Article 158346

Journal of Alloys and Compounds
Supports *open access*

Menu

7.6 CiteScore
4. In

Article 158487

Purchase PDF Article preview

Research article ○ Abstract only

Large electric-field-induced strain and energy storage properties in $Bi_{0.5}Na_{0.5}TiO_3$-($0.5Ba_{0.7}Ca_{0.3}TiO_3$-$0.5BaTi_{0.8}Zr_{0.2}O_3$) lead-free relaxor ferroelectric ceramics

Peng Shi, Tangyuan Li, Xiaojie Lou, Zhonghai Yu, ... Sen Yang

Article 158369

Purchase PDF Article preview

Research article ○ Abstract only

Microstructure refinement and enhanced tensile properties of Al-11Mg_2Si alloy modified by erbium

Ke-Yan Wang, Jun Xiang, Rong-Da Zhao, Jin-Liang Bi, ... Jürgen Eckert

Article 158421

Purchase PDF Article preview

Research article ○ Abstract only

Polyol-mediated synthesis of Bi-deficient Mg^{2+}-doped sodium bismuth titanate and study of oxide ion migration behavior with functional properties

Pragati Singh, Raghvendra Pandey, Prabhakar Singh

Article 158492

Purchase PDF Article preview

Research article ○ Abstract only

$ZnFe_2O_4$ nanorods on reduced graphene oxide as advanced supercapacitor electrodes

Mohammad Bagher Askari, Parisa Salarizadeh, Majid Seifi, Mohammad Hassan Ramezan zadeh, Antonio Di Bartolomeo

Article 158497

Purchase PDF Article preview

Research article ○ Abstract only

Epitaxial growth of cubic WC_y(001) on MgO(001)

Peijiao Fang, Baiwei Wang, C.P. Mulligan, T.M. Murray, ... Daniel Gall

Article 158403

Purchase PDF Article preview

Research article ○ Abstract only

Ultra-high strength Co–Ta–B bulk metallic glasses: Glass formation, thermal stability and crystallization

Ju Wang, Ivan Kaban, Volodymyr Levytskyi, Ran Li, ... Kornelius Nielsch

Article 158398

Purchase PDF Article preview

Research article ○ Abstract only

Journal of Alloys and Compounds
Supports *open access*

Menu

7.6 CiteScore 4. In

Research article ○ Abstract only

Influence of A- and B-site substitutions on crystal structure and oxygen content in air-prepared $Ba_{1-x}Pr_xFe_{1-y}Co_yO_{3-\delta}$ perovskites

N.E. Volkova, M.V. Bazueva, D.T. Aisarinova, A.D. Alkhamova, ... A. Maignan

Article 158438

Purchase PDF Article preview

Research article ○ Abstract only

Synthesis, characterization, and photocatalytic activity of stannum-doped $MgIn_2S_4$ microspheres

Wenhong Yang, Yujing Dong, Zhipeng Wang, Yuqin Li, ... Chao Zeng

Article 158446

Purchase PDF Article preview

Research article ○ Abstract only

Heat capacity of samarium titanates and phase equilibria of Sm_2O_3-TiO_2 system

Weiping Gong, Yanzhi Liu, Zhihong Luo

Article 158429

Purchase PDF Article preview

Research article ○ Abstract only

Rod-shaped α-MnO_2 electrocatalysts with high Mn^{3+} content for oxygen reduction reaction and Zn-air battery

Chenrui Shao, Kui Yin, Fan Liao, Wenxiang Zhu, ... Mingwang Shao

Article 158427

Purchase PDF Article preview

Research article *Open access*

Effects of ZrC content on the microstructure and mechanical property of ZrC/ZTA composites consolidated by hot pressing

Shufen Li, Yabin Zhu, Jianlong Chai, Yiwen Liu, ... Erqing Xie

Article 158402

Download PDF Article preview

Research article ○ Abstract only

$Sr_4Al_{14}O_{25}$: Eu^{2+}, Dy^{3+}@ZnO nanocomposites as highly efficient visible light photocatalysts for the degradation of aqueous methyl orange

Samvit G. Menon, A.K. Bedyal, Trilok Pathak, Vinay Kumar, Hendrik C. Swart

Article 158370

Purchase PDF Article preview

Research article ○ Abstract only

Study on the microwave absorbing properties of Fe nanoparticles prepared by the HEIBE method in expanded graphite matrix composites

Yaoxu Zhu, Deren Li, Zhiguo Wu, Shurong Xu, ... Penxun Yan

Journal of Alloys and Compounds
Supports *open access*

Menu

7.6 CiteScore

medium for fuel cell applications
Kaaviah Manoharan, Vasantha Kumar Palaniswamy, Kannan Raman, Rajashabala Sundaram
Article 158444

Purchase PDF Article preview

Research article ○ Abstract only
A hierarchical composites constructed by ZIF-8 derived carbon core and Mn_3O_4/N-doped carbon shell as efficient polysulfide entrapment host for Li–S batteries
Zhipeng Sun, Lujun Fang, Junjie Cai
Article 158461

Purchase PDF Article preview

Research article ○ Abstract only
$Ti_2Nb_2O_9$/graphene hybrid anode with superior rate capability for high-energy-density sodium-ion capacitors
Liaona She, Feng Zhang, Congying Jia, Liping Kang, ... Zong-Huai Liu
Article 158431

Purchase PDF Article preview

Research article ○ Abstract only
N,S co-doped carbon confined MnO/MnS heterostructures derived from a one-step pyrolysis of Mn-methionine frameworks for advanced lithium storage
Kui Wang, Kangjia Zhao, Yaping Wang, Huanhuan Li, ... Long Chen
Article 158451

Purchase PDF Article preview

Research article ○ Abstract only
Absorption and emission in the visible range by ultra-small PbS quantum dots in the strong quantum confinement regime with S-terminated surfaces capped with diphenylphosphine
Nayely Torres-Gomez, Diana F. Garcia-Gutierrez, Alan R. Lara-Canche, Lizbeth Triana-Cruz, ... Domingo I. Garcia-Gutierrez
Article 158443

Purchase PDF Article preview

Research article ○ Abstract only
Local environment of iron and tin ions, diffuse absorption, and giant dielectric response in $BaFe_{1/2}Sn_{1/2}O_{3-\delta}$ prepared by the sol-gel method
E.A. Bikyashev, S.P. Kubrin, A.V. Popov, A.V. Pavlenko, ... N.V. Ter-Oganessian
Article 158327

Purchase PDF Article preview

Research article ○ Abstract only
Nanostructured Te–SnTe eutectic composites with enhanced thermoelectric performance
Bin Yang, Shuangming Li, Xin Li, Zhenpeng Liu, ... Songke Feng

Journal of Alloys and Compounds
Supports *open access*

Menu

7.6 CiteScore

alloy
Abbas Ahmadi Siahboumi, Ahmad Kermanpur, Fazlollah Sadeghi, Hamid Reza Ghorbani
Article 158437

Purchase PDF Article preview

Research article ○ Abstract only
Facile synthesis of rGO/Ag@AgCl core-shells nanocomposite and their multifunctional efficacy as a photocatalyst and antimicrobial agent for decontamination of water
Th.Babita Devi, M. Ahmaruzzaman
Article 157988

Purchase PDF Article preview

Research article ○ Abstract only
Ultrathin, biomimetic multifunctional leaf-like silver nanowires/Ti_3C_2Tx MXene/cellulose nanofibrils nanocomposite film for high-performance electromagnetic interference shielding and thermal management
Qing Liu, Yi Zhang, Yibin Liu, Zongxu Liu, ... Qiuyu Zhang
Article 158151

Purchase PDF Article preview

Research article ○ Abstract only
Crystal structure and phase transitions at high pressures in the superconductor $FeSe_{0.89}S_{0.11}$
Yulia A. Nikiforova, Anna G. Ivanova, Kirill V. Frolov, Igor S. Lyubutin, ... Mahmoud Abdel-Hafiez
Article 158419

Purchase PDF Article preview

Research article ○ Abstract only
Microstructure and mechanical properties of two uranium-containing high-entropy alloys
Jie Shi, He Huang, Guichao Hu, Pengguo Zhang, ... Chao Luo
Article 158295

Purchase PDF Article preview

Research article ○ Abstract only
Selective and efficient extraction of Nd from NdFeB magnets via ionization in LiCl-KCl-$CdCl_2$ melt
Younghwan Jeon, Jungho Hur, Gwan Yoon Jeong, Sungjune Sohn, Jaeyeong Park
Article 158424

Purchase PDF Article preview

Research article ○ Abstract only
An efficient platform based on strontium titanate nanocubes interleaved polypyrrole nanohybrid as counter electrode for dye-sensitized solar cell
Usman Ahmed, M.M. Shahid, Syed Shahabuddin, Nasrudin Abd Rahim, ... Suresh Sagadevan
Article 158228

Journal of Alloys and Compounds
Supports *open access*

Menu

7.6 CiteScore 4. In

Hesam Pouraliakbar, Sang Hun Shim, Yong Keun Kim, Mohsen Saboktakin Rizi, ... Sun Ig Hong
Article 158412

Purchase PDF Article preview

Research article ○ Abstract only
Ti_3Al matrix alloy refined and reinforced by *in-situ* synthesized SiC_w/Nb_4C_3 core-shell structure
Sen Cui, Chunxiang Cui, Licong Kang, Shuangjin Liu
Article 158423

Purchase PDF Article preview

Research article ○ Abstract only
Tetragonal to cubic transition of $Sr_{0.8}Dy_{0.2}CoO_{3-\delta}$ and oxygen mobility: TG-DSC-XRD study
Sergei Vereshchagin, Vyacheslav Dudnikov, Yury Orlov, Leonid Solovyov
Article 158257

Purchase PDF Article preview

Research article ○ Abstract only
A novel three-dimensional cross-linked net structure of submicron Si as high-performance anode for LIBs
Junhua Liang, Zhengqing Fan, Si Chen, Songsheng Zheng, Zhaolin Wang
Article 158433

Purchase PDF Article preview

Research article ○ Abstract only
Aging behavior of Haynes® 282® wrought nickel superalloy subjected to a cold pre-deformation by differential speed rolling
Wojciech Polkowski, Adelajda Polkowska, Sebastian Lech
Article 158418

Purchase PDF Article preview

Research article ○ Abstract only
Evaluating compressive property and hot deformation behavior of molybdenum alloy reinforced by nanoscale zirconia particles
Liujie Xu, Tielong Sun, Yucheng Zhou, Fangnao Xiao, ... Shizhong Wei
Article 158289

Purchase PDF Article preview

Research article ○ Abstract only
On the influence of AgMg precursor formation on MgAgSb microstructure and thermoelectric properties
Ignacio Rodriguez-Barber, Julia Camut, Laura Luhmann, Aidan Cowley, ... Johannes de Boor
Article 158384

Purchase PDF Article preview

Research article ○ Abstract only
Enlarging heat-treatment processing windows of Fe–Si–B–P–Cu–M nanocrystalline alloys by doping transition metal elements

Journal of Alloys and Compounds
Supports *open access*

Menu

7.6 CiteScore
4. In

The energy-storage performance and dielectric properties of (0.94-x)BNT-0.06BT-xST thin films prepared by sol–gel method
Yanjiang Xie, Hua Hao, Juan Xie, Zichen He, ... Hanxing Liu
Article 158164

Purchase PDF Article preview

Research article ○ Abstract only
Effects of Li_2O_2 on structure and electrochemical properties of $LiNi_{0.88}Co_{0.09}Al_{0.03}O_2$ cathode materials
Shibo Shang, Xianyou Wang, Feng Jiang
Article 158262

Purchase PDF Article preview

Research article ○ Abstract only
A gleeble-assisted study of phase evolution of Ti-6Al-4V induced by thermal cycles during additive manufacturing
Yaohong Xiao, Matt Cagle, Shiraz Mujahid, Pengwei Liu, ... Lei Chen
Article 158409

Purchase PDF Article preview

Research article ○ Abstract only
Ultra-micro amperometric sensor of isoniazid using carbon doped vanadium trioxide @ Prussian blue supported on graphite felt
Qiangming Wang, Jihua Zhao, Simon Tricard, Jian Fang
Article 158176

Purchase PDF Article preview

Research article ○ Abstract only
Highly sensitive ammonia gas sensor based on metal-organic frameworks-derived $CoSe_2$@nitrogen-doped amorphous carbon decorated with multi-walled carbon nanotubes
Qian Mi, Dongzhi Zhang, Xixi Zhang, Dongyue Wang
Article 158252

Purchase PDF Article preview

Research article ○ Abstract only
Phase transformation and microstructure evolution of a beta-solidified gamma-TiAl alloy
Haitao Huang, Hongsheng Ding, Xuesong Xu, Ruirun Chen, ... Hengzhi Fu
Article 158082

Purchase PDF Article preview

Research article ○ Abstract only
Deformation modes and yield strength anomaly in $L1_2$ compounds
K.V. Vamsi, S. Karthikeyan
Article 158411

Purchase PDF Article preview

Journal of Alloys and Compounds
Supports *open access*

Menu

7.6 CiteScore
4. In

Purchase PDF Article preview

Research article ○ Abstract only

DFT insights into new B-containing 212 MAX phases: Hf_2AB_2 (A = In, Sn)

M.A. Ali, M.M. Hossain, M.M. Uddin, A.K.M.A. Islam, ... S.H. Naqib

Article 158408

Purchase PDF Article preview

Research article ○ Abstract only

A coordinated regulation strategy to improve electronic conductivity and Li-ion transport for TiO_2 lithium battery anode materials

Yicheng Fan, Xuhui Chen, Kun Zhang, Ju Rong, Xiaohua Yu

Article 158282

Purchase PDF Article preview

Research article ○ Abstract only

GaN/Al_2O_3 core-shell nanowire based flexible and stable piezoelectric energy harvester

Aadil Waseem, Muhammad Ali Johar, Mostafa Afifi Hassan, Indrajit V. Bagal, ... Sang-Wan Ryu

Article 158545

Purchase PDF Article preview

Research article ○ Abstract only

Structural, physical and radiation attenuation properties of tungsten doped zinc borate glasses

H.A. Saudi, W.M. Abd-Allah

Article 158225

Purchase PDF Article preview

Research article ○ Abstract only

In situ dual matrix composite with segregated microstructure fabricated from Al–TiO_2–B_2O_3 system by mechanical thermal process

Suprabha Lakra, Tapas Kumar Bandyopadhyay, Siddhartha Das, Karabi Das

Article 158527

Purchase PDF Article preview

Research article ○ Abstract only

Tunneling conduction mechanisms in strontium ferromolybdate ceramics with strontium molybdate dielectric intergrain barriers

Gunnar Suchaneck, Nikolay Kalanda, Evgenij Artiukh, Marta Yarmolich, Nikolai A. Sobolev

Article 158526

Purchase PDF Article preview

Research article ○ Abstract only

Journal of Alloys and Compounds
Supports *open access*

Menu

7.6 CiteScore 4. In

Research article ○ Abstract only

Hot deformation behavior and microstructural evolution of supersaturated Inconel 783 superalloy

Ke Tang, Zhibo Zhang, Jin Tian, Yake Wu, Feng Jiang

Article 158541

Purchase PDF Article preview

Research article ○ Abstract only

Hydrogen enhancing Ga doping efficiency and electron mobility in high-performance transparent conducting Ga-doped ZnO films

Anh Tuan Thanh Pham, Dung Van Hoang, Truong Huu Nguyen, Oanh Kieu Truong Le, ... Vinh Cao Tran

Article 158518

Purchase PDF Article preview

Research article ○ Abstract only

Crystal growth, optical, luminescence and scintillation characterization of $Li_2Zn_2(MoO_4)_3$ crystal

Indra Raj Pandey, Sujita Karki, D. Joseph Daniel, H.J. Kim, ... V.A. Trifonov

Article 158510

Purchase PDF Article preview

Research article ○ Abstract only

Effects of oxidized Ketjen Black as conductive additives on electrochemical performance of the $LiMn_2O_4@Al_2O_3$ cathode in lithium-ion batteries

Hongqiang Wang, Jinlu Han, Lianxiao Li, Fan Peng, ... Qingyu Li

Article 158482

Purchase PDF Article preview

Research article ○ Abstract only

Optical and scintillation properties of Nd-doped $Lu_2Si_2O_7$ single crystals

Prom Kantuptim, Masaki Akatsuka, Daisuke Nakauchi, Takumi Kato, ... Takayuki Yanagida

Article 158538

Purchase PDF Article preview

Research article ○ Abstract only

Correlation between microstructural characteristics and cavitation resistance of Stellite-6 coatings on 17-4 PH stainless steel prepared with supersonic laser deposition and laser cladding

Qunli Zhang, Lijuan Wu, Hongsen Zou, Bo Li, ... Jianhua Yao

Article 158417

Purchase PDF Article preview

Research article ○ Abstract only

Interfacial heat transfer and microstructural analyses of a Bi- 5% Sb lead-free alloy solidified against Cu, Ni and low-C steel substrates

Journal of Alloys and Compounds
Supports *open access*

Menu

7.6 CiteScore
4. In

Textural evolution and improved ductility in Zn-0.2Mg-0.8Mn (wt%) alloys at different extrusion temperatures
Dongfang Lou, Liqing Wang, Yuping Ren, Hongxiao Li, Gaowu Qin
Article 158530

Purchase PDF Article preview

Research article ○ Abstract only
Modeling texture evolution during monotonic loading of Zn-Cu-Ti alloy sheet using the viscoplastic self-consistent polycrystal model
A. Roatta, M. Leonard, E. Nicoletti, J.W. Signorelli
Article 158425

Purchase PDF Article preview

Research article ○ Abstract only
Structural stability of mechanically alloyed amorphous $(FeCoNi)_{70}Ti_{10}B_{20}$ under high-temperature and high-pressure
Baris Avar, Tuncay Simsek, Sadan Ozcan, Arun K. Chattopadhyay, Bora Kalkan
Article 158528

Purchase PDF Article preview

Research article ○ Abstract only
Energy transfer study in $GdVO_4$: Bi^{3+}, Yb^{3+} obtained by microwave-assisted hydrothermal method
Katarzyna Lenczewska, Maciej Ptak, Vitalii Boiko, Karolina Ledwa, Dariusz Hreniak
Article 158393

Purchase PDF Article preview

Research article ○ Abstract only
Effect of mechanical milling on the harmonic structure development during spark plasma sintering of Ti-5Al-2Sn-4Zr-4Mo-2Cr-1Fe β-metastable titanium alloy (β-Cez alloy)
Bhupendra Sharma, Benoît Denand, Petr Harcuba, Guillaume Geandier, ... Elisabeth Aeby-Gautier
Article 158483

Purchase PDF Article preview

Research article ○ Abstract only
Insight into the transport properties and enhanced thermoelectric performance of *n*-type $Pb_{1-x}Sb_xTe$
Taras Parashchuk, Ihor Horichok, Artur Kosonowski, Oleksandr Cherniushok, ... Krzysztof T. Wojciechowski
Article 158355

Purchase PDF Article preview

Research article ○ Abstract only
Structure-property relationships in the lanthanide-substituted $PbBi_2Nb_2O_9$ Aurivillius phase synthesized by the molten salt method
Tio Putra Wendari, Syukri Arief, Nandang Mufti, Andon Insani, ... Zulhadjri
Article 158440

Journal of Alloys and Compounds
Supports *open access*

Menu

7.6 CiteScore
4. In

Chen Chen, Boyuan Ban, Jifei Sun, Jingwei Li, ... Seyed Hadi Tabaian
Article 158517

Purchase PDF Article preview

Research article ○ Abstract only
Porous sulfurized poly(acrylonitrile) nanofiber as a long-life and high-capacity cathode for lithium–sulfur batteries
Keyao Wang, Shunlong Ju, Qili Gao, Guanglin Xia, ... Xuebin Yu
Article 158445

Purchase PDF Article preview

Research article ○ Abstract only
Effect of B on improving wetting and imbibition of sintered porous Ta by Cu melt
S.N. Zhevnenko, M.V. Gorshenkov, I.S. Petrov
Article 157886

Purchase PDF Article preview

Research article ○ Abstract only
Microstructure and properties of dual-scale particulate reinforced copper matrix composites with superior comprehensive properties
Siruo Zhang, Huijun Kang, Zhicheng Wang, Enyu Guo, ... Tongmin Wang
Article 157888

Purchase PDF Article preview

Research article ○ Abstract only
Synthesis of well dispersed NiO ink for efficient perovskite solar cells
Tonghui Guo, Zequn Zhang, Luting Yu, Haobo Yuan, ... Yuejin Zhu
Article 157889

Purchase PDF Article preview

Research article ○ Abstract only
Improvement of the magnetic properties of $SrFe_{12}O_{19}$ ceramics by tailored sintering with SiO_2 addition
J.C. Guzmán-Mínguez, L.M. Vicente-Arche, C. Granados-Miralles, J.F. Fernández, A. Quesada
Article 157890

Purchase PDF Article preview

Research article ○ Abstract only
The abnormal multiple dielectric relaxation responses of Al^{3+} and Nb^{5+} co-doped rutile TiO_2 ceramics
Xiao-gang Zhao, Lin Chen, Xiang-yu Zhang, Peng Liu, ... Gang Shi
Article 157891

Purchase PDF Article preview

Research article ○ Abstract only

Journal of Alloys and Compounds

Supports *open access*

Menu

7.6 CiteScore

4. In

page 1 of 2

Previous vol/issue

Next vol/issue

Journal of Alloys and Compounds 860 (2021) 158440

Contents lists available at ScienceDirect

Journal of Alloys and Compounds

journal homepage: www.elsevier.com/locate/jalcom

Structure-property relationships in the lanthanide-substituted $PbBi_2Nb_2O_9$ Aurivillius phase synthesized by the molten salt method

Tio Putra Wendari[a], Syukri Arief[a], Nandang Mufti[b], Andon Insani[c], Jacob Baas[d], Graeme R. Blake[d], Zulhadjri[a,*]

[a] Department of Chemistry, Faculty of Mathematics and Natural Sciences, Universitas Andalas, Kampus Limau Manis, Padang 25163, Indonesia
[b] Department of Physics, Faculty of Mathematics and Natural Sciences, Universitas Negeri Malang, Jl. Semarang 5, Malang 65145, Indonesia
[c] Center for Science and Technology of Advanced Materials, National Nuclear Energy Agency of Indonesia, Puspiptek Serpong, Tangerang Selatan 15314, Indonesia
[d] Zernike Institute for Advanced Materials, University of Groningen, Nijenborgh 4, 9747 AG Groningen, The Netherlands

ARTICLE INFO

Article history:
Received 30 September 2020
Received in revised form 4 November 2020
Accepted 20 December 2020
Available online 23 December 2020

Keywords:
Aurivillius phase
Structural analysis
Cation disorder
Rare-earth substitution
Ferroelectric properties

ABSTRACT

Samples of $PbBi_2Nb_2O_9$, $PbBi_{1.5}La_{0.5}Nb_2O_9$, and $PbBi_{1.5}Nd_{0.5}Nb_2O_9$ have been prepared by the molten salt method. The structure, morphology, and electrical properties were investigated. All samples are single-phase and crystallize in an orthorhombic structure with $A2_1am$ symmetry. Neutron diffraction data indicate that the Ln^{3+} cations prefer to occupy the perovskite *A*-site, whereas Pb/Bi occupy the perovskite *A*-site and the Bi_2O_2 layer. Changes in unit cell volume are observed on substitution and are attributed to the ionic radii of the Ln^{3+} cations and also correlated to changes in the *B*-O bond distances in the BO_6 octahedra, which are also observed in IR spectra. SEM images reveal anisotropic plate-like grains, which increase in size with the presence of Ln^{3+} ions. The ferroelectric transition temperature (T_c) decreases with decreasing degree of BO_6 distortion as the influence of the $6s^2$ lone pair of Bi^{3+} is diminished. Relaxor ferroelectric behavior is observed with Ln^{3+} substitution, driven by the disorder of the *A*-site cations. The room temperature ferroelectric polarization increases with Ln^{3+} substitution, ascribed to the decreased dielectric loss.

1. Introduction

The ferroelectric Aurivillius phases have received continued attention over the past few decades because of potential uses in non-volatile ferroelectric random access memory, energy storage, piezoelectric device applications, and high-temperature ferroelectric devices [1–4]. The crystal structure of Aurivillius phases can be described as an *m*-perovskite layer $[A_{m-1}B_mO_{3m+1}]^{2-}$ sandwiched between bismuth oxide $[Bi_2O_2]^{2+}$ layers along the *c*-axis. The integer m represents the number of BO_6 octahedra in the perovskite slab, which can accommodate various *A*-site and *B*-site cations, where *A* is a mono-, di-, or trivalent cation (or a combination thereof suited to dodecahedral coordination) and *B* is a transition metal cation suited to octahedral coordination [5].

Lead bismuth niobate, $PbBi_2Nb_2O_9$ (PBNO), is a typical double-layer (m = 2) Aurivillius phase exhibiting a high dielectric constant together with a high ferroelectric Curie temperature (T_c) of 830 K [6]. The ferroelectric properties are due to the $6s^2$ lone pair electrons associated with Pb^{2+} and Bi^{3+}, which induce a highly distorted structure. However, the spontaneous polarization is relatively low with a high coercive field, hindering possible application in the field of piezoelectric devices and energy storage [3,7].

Recently, efforts have been made to enhance its electrical properties by chemical modification of the *A*- or *B*-site cations, or both simultaneously, which can manipulate the structure as well as the properties. Due to the large range of *A*-site ionic radii that can be incorporated in the structure, the substitution of *A*-site cations is a feasible way to obtain more distorted BO_6 octahedra and hence enhance the ferroelectricity [8]. It has also been demonstrated that the substitution of Ln^{3+} for Bi^{3+} suppresses the oxygen vacancy concentration as well as leakage currents, consequently improving the ferroelectric properties [9,10]. Substitution also results in cation disorder, which can give rise to relaxor behavior and greater potential for use in various electronic devices [11].

Most studies have reported on the substitution of Ln^{3+} for Bi^{3+} in double-layer Aurivillius compound $SrBi_2Nb_2O_9$, which is likely to lower T_c [12–14]. However, the detailed structural changes that occur on substitution, including the cation distribution, which is strongly correlated to the reduced T_c, has thus far been less investigated. Since ferroelectricity can be realized by structural

* Corresponding author.
E-mail address: zulhadjri@sci.unand.ac.id (Zulhadjri).

https://doi.org/10.1016/j.jallcom.2020.158440
0925-8388/

features such as atomic displacements and tilting of the BO_6 octahedra [15], it is important to determine precisely the positions of each atom, especially the light oxygen atoms.

In this work, we have synthesized the double-layer Aurivillius compound $PbBi_2Nb_2O_9$ and partially substituted lanthanide ions (*Ln*: La^{3+} and Nd^{3+}) using the molten-salt method, which has not previously been reported. The La^{3+} and Nd^{3+} ions were chosen to represent a larger and smaller cation compared to Bi^{3+} since the different size of the substituting ions is expected to lead to different types of structural distortion. We therefore synthesized compounds of composition $PbBi_2Nb_2O_9$, $PbBi_{1.5}La_{0.5}Nb_2O_9$, and $PbBi_{1.5}Nd_{0.5}Nb_2O_9$, abbreviated as PBNO, PBNO-La and PBNO-Nd, respectively. We perform neutron diffraction on these compounds and focus on the detailed structural changes, including compositional disorder, in order to further understand the correlation of the structure with the dielectric and ferroelectric properties.

2. Experimental procedures

The samples of PBNO, PBNO-La and PBNO-Nd were prepared by the molten salt method using K_2SO_4/Na_2SO_4 salt fluxes. High purity oxide precursors of PbO, Bi_2O_3, La_2O_3, Nd_2O_3, and Nb_2O_5 (Aldrich, ≥ 99.99%) were weighed in stoichiometric proportions and ground in an agate mortar in ethanol. The oxide precursors then were ground together with a 1:1 molar ratio of K_2SO_4/Na_2SO_4 (Aldrich, ≥ 99%) salts with a molar ratio of 1:7 salt to oxide and placed in alumina crucibles. The mixtures were heated at a rate of 5 K/min to 1023 K, 1123 K, and 1223 K and held for 5 h at each temperature, with intermediate grinding steps. The final products were washed thoroughly with hot distilled water to remove the sulfate fluxes and dried at 383 K for 5 h. The crystalline phases were identified using X-ray powder diffraction (XRD; Shimadzu XRD 7000 operating with Cu Kα radiation) at room temperature. Neutron powder diffraction (NPD) data were collected on the High-Resolution Powder Diffractometer (DN3) at the Center for Science and Technology of Advanced Materials, BATAN, Indonesia. The wavelength of the incident neutron beam was 1.8195 Å and data were collected for 11 h at room temperature. The unit cell parameters, site occupations, and atomic positions were refined by the Rietveld method from the NPD data using the RIETICA program [16]. FTIR spectra were obtained with a Perkin Elmer 1600 FTIR spectrophotometer at room temperature. Scanning electron microscopy (SEM; FEI INSPECT S50) was used to investigate the microstructures of the samples. For electrical measurements, the final product was mixed with 5 wt% PVA as a binder and pressed to form a pellet. The pellet was slowly heated at 773 K for 3 h to burn out the binder and then continuously sintered at 1323 K for 5 h. The densities of the pellets were measured using the Archimedes method and the theoretical densities were obtained from the NPD analysis. Silver electrode paste (Aldrich, 99%) was coated on both surfaces of the sintered pellet and then heated at 383 K for 2 h. The temperature dependence of the dielectric constant and dielectric loss was measured over the frequency range 50 kHz to 1 MHz at temperatures between 300 K and 850 K using an LCR meter (Agilent E4980A). Room-temperature polarization loops were measured using a ferroelectric test system (TF Analyzer, AixACCT) at 1 Hz as a function of the applied electric field.

3. Results and discussion

Fig. 1 shows the XRD patterns of the PBNO, PBNO-La, and PBNO-Nd samples at room temperature. The XRD patterns are indexed according to a $PbBi_2Nb_2O_9$ standard diffraction pattern with the orthorhombic $A2_1am$ space group (ICSD-95920). All three XRD patterns show the typical peaks of the double-layered Aurivillius phase without any additional peaks, confirming the formation of single-phase products. The most intense diffraction peak (1 1 5) for all three samples is typical for double-layer Aurivillius phases (m = 2), which is in agreement with the fact that the most intense reflection is (1 1 2m+1) [17,18]. The XRD results thus demonstrate that the substitution of 25% molar ratio La^{3+} or Nd^{3+} for Bi^{3+} in $PbBi_2Nb_2O_9$ was successful.

It is observed in the enlarged XRD patterns in Fig. 1 that the 200/020 doublet of the PBNO sample at 2θ = 32–33° is typical for the $A2_1am$ orthorhombic crystal structure [19,20]. With Ln^{3+} substitution, these peaks almost merge to a single peak in both cases, which indicates that the structure becomes close to tetragonal [18,20]. This change in the degree of orthorhombicity can also be expected to affect the ferroelectric properties, as discussed further below. Additionally, the main XRD peaks slightly shift toward lower 2θ for PBNO-La and toward higher 2θ for PBNO-Nd, corresponding to changes in the lattice parameters [21].

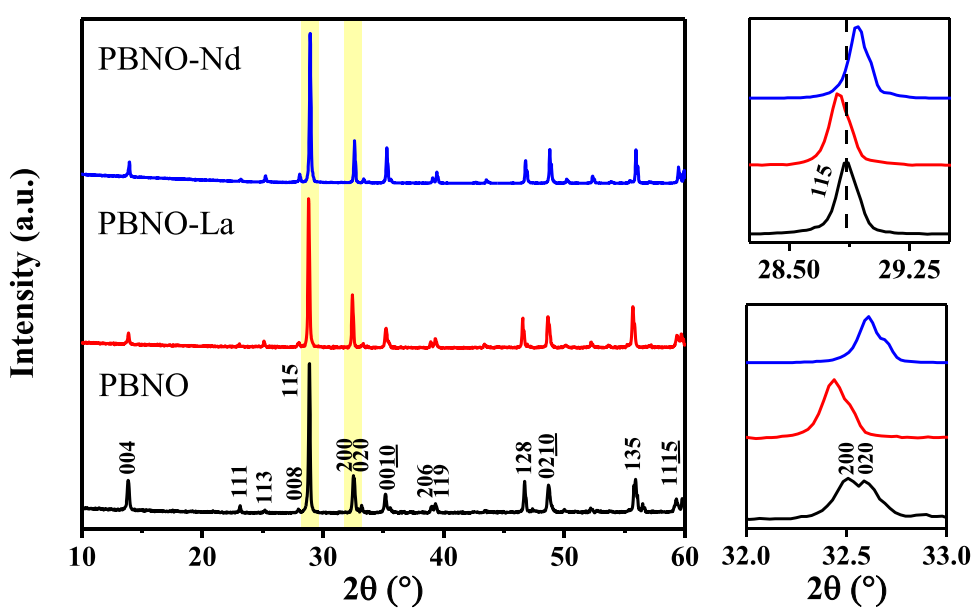

Fig. 1. Room temperature X-ray diffraction patterns of pristine $PbBi_2Nb_2O_9$ and La, Nd-substituted samples.

Rietveld refinement of the NPD data was performed to investigate the structural parameters in detail. The initial refinements considered the structural model where $PbBi_2Nb_2O_9$ adopts the $A2_1am$ space group (ICSD-88479). All atoms occupy general Wyckoff positions 8b except for Bi(1) and O(1) in the perovskite layer which occupy 4a positions. Further to be noted, a result of the substitution of Ln^{3+} for Bi^{3+} is that there is insufficient Bi^{3+} to form the Bi_2O_2 layer, and consequently the other *A*-site cations (Pb^{2+}, La^{3+} or Nd^{3+}) should partially occupy the Bi-site. According to earlier studies, the occupation of the Bi_2O_2 layer by Ln^{3+} cations is not favored [19,22,23]. However, cations with a stereochemically active $6s^2$ lone pair similar to Bi^{3+} can possibly occupy this site [24]. Therefore, we assumed that Pb^{2+} can be incorporated into the Bi-site of the Bi_2O_2 layer, and the occupation by Ln^{3+} was assumed to be zero.

The refinement was initially performed with all Bi^{3+} cations occupying the *A*(2)-site of the Bi_2O_2 layer for PBNO. For the PBNO-La and PBNO-Nd samples, we performed refinements where all Ln^{3+} cations were confined to the *A*(1)-site of the perovskite layer with a 50% occupancy. The partial occupancy of the *A*(2)-site of the Bi_2O_2 layer by the Ln^{3+} cations was also considered but led to significantly worse fits. The positions of Nb and O atoms in the perovskite layer were refined while constraining the occupation to 1. Furthermore, the disorder of Pb^{2+} and Bi^{3+} cations in both layers should be considered in the refinement. The Pb/Bi disorder on both the *A*(1)-site of the perovskite layer and the *A*(2)-site of the Bi_2O_2 layer was refined by varying the occupancies manually, whereas the atomic positions were refined automatically. The final Rietveld fits of the NPD data are shown in Fig. 2(a). The detailed atomic positions and occupancies of the atoms are listed in Table 1.

The refinement results indicate that the Ln^{3+} ions only occupy the *A*(1)-site in the perovskite layer, together with Pb^{2+} and Bi^{3+}. The *A*(2)-site in the Bi_2O_2 layers is only occupied by Pb^{2+} and Bi^{3+}. This type of disorder is expected due to the preference of Ln^{3+} to occupy the *A*(1)-site of the perovskite layer rather than the *A*(2)-site of the Bi_2O_2 layer since the Ln^{3+} ions lack the necessary lone pair electrons

Table 1
Atomic coordinates and occupancies of all three samples obtained from Rietveld refinements using NPD data at room temperature.

Atom	Site	*x*	*y*	*z*	Occ
PBNO					
Pb(1)	4a	0	0.242(5)	0	0.880
Bi(1)	4a	0	0.242(5)	0	0.120
Bi(2)	8b	0.475(8)	0.744(4)	0.2013(4)	0.940
Pb(2)	8b	0.475(8)	0.744(4)	0.2013(4)	0.060
Nb(1)	8b	0.476(8)	0.764(5)	0.4117(5)	1
O(1)	4a	0.449(2)	0.191(7)	0	1
O(2)	8b	0.432(9)	0.800(5)	0.3405(7)	1
O(3)	8b	0.695(9)	0.0059(7)	0.25	1
O(4)	8b	0.661(9)	0.955(8)	0.0793(1)	1
O(5)	8b	0.728(10)	0.982(8)	0.5756(1)	1
PBNO-La					
Pb(1)	4a	0	0.246(9)	0	0.300
Bi(1)	4a	0	0.246(9)	0	0.200
La(1)	4a	0	0.246(9)	0	0.500
Bi(2)	8b	0.5057(12)	0.744(5)	0.1994(6)	0.700
Pb(2)	8b	0.5057(12)	0.744(5)	0.1994(6)	0.300
Nb(1)	8b	0.4643(8)	0.725(8)	0.4138(7)	1
O(1)	4a	0.444(7)	0.1950(13)	0	1
O(2)	8b	0.442(2)	0.7515(14)	0.3405(10)	1
O(3)	8b	0.7117(11)	0.0081(11)	0.25	1
O(4)	8b	0.6983(15)	0.958(9)	0.0795(17)	1
O(5)	8b	0.738(3)	0.993(3)	0.5727(17)	1
PBNO-Nd					
Pb(1)	4a	0	0.2330(16)	0	0.350
Bi(1)	4a	0	0.2330(16)	0	0.150
Nd(1)	4a	0	0.2330(16)	0	0.500
Bi(2)	8b	0.4953(16)	0.737(5)	0.2002(5)	0.675
Pb(2)	8b	0.4953(16)	0.737(5)	0.2002(5)	0.325
Nb(1)	8b	0.462(3)	0.730(6)	0.4147(6)	1
O(1)	4a	0.444(2)	0.196(16)	0	1
O(2)	8b	0.473(4)	0.766(8)	0.3444(9)	1
O(3)	8b	0.738(14)	0.0053(3)	0.25	1
O(4)	8b	0.6912(2)	0.9771(11)	0.0769(11)	1
O(5)	8b	0.723(2)	0.9733(17)	0.5644(11)	1

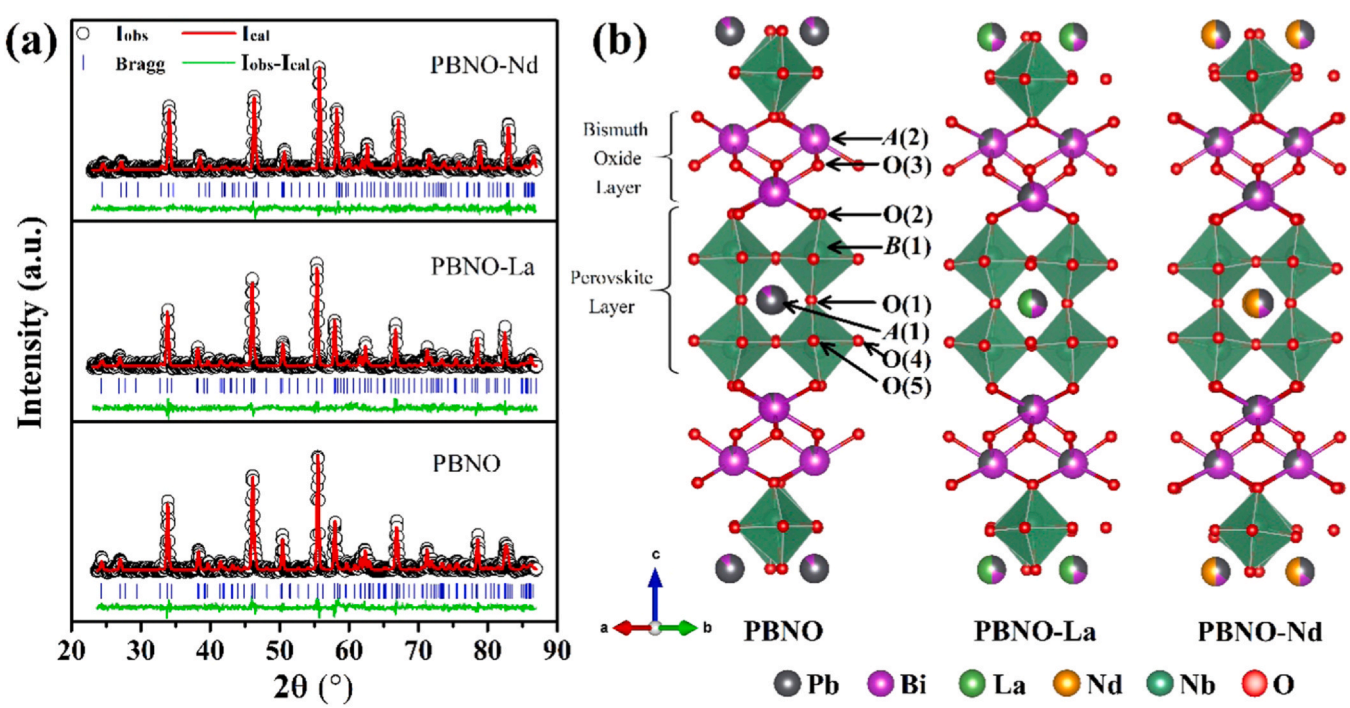

Fig. 2. (a) Observed, calculated and difference NPD profiles at room temperature. (b) Crystal structure models viewed along the [110] direction showing the occupation of each cation in the Bi_2O_2 and perovskite layers.

Table 2
Refined unit cell parameters, volume, orthorhombicity parameter and fit parameters of samples determined from NPD data at room temperature using the orthorhombic space group $A2_1am$.

	PBNO	PBNO-La	PBNO-Nd
Space group	$A2_1am$	$A2_1am$	$A2_1am$
Crystal class	Orthorhombic	Orthorhombic	Orthorhombic
a (Å)	5.4923(7)	5.4977(1)	5.4794(3)
b (Å)	5.4764(2)	5.4955(9)	5.4759(5)
c (Å)	25.4321(1)	25.4489(2)	25.3561(6)
V (Å^3)	764.974(8)	768.878(7)	760.801(1)
$(a-b)/(a+b)$	0.00145	0.00019	0.00032
Z	4	4	4
R_p	13.34	14.89	14.13
χ^2	1.667	1.517	1.475

[15,22]. Similar Pb/Bi disorder in $PbBi_2Nb_2O_9$ was previously reported by Ismunandar et al. [24]. The occupation of Bi^{3+} on the $A(1)$-site of the perovskite layer is similar for all three samples: 12% for PBNO, 10% for PBNO-La, and 15% for PBNO-Nd. The slight increase of Bi^{3+} occupation in the perovskite layer for PBNO-Nd might be a result of the smaller Nd^{3+} cation decreasing the average size of the BO_6 octahedra, leading to a greater preference for the Bi^{3+} ions, which are slightly smaller than Pb^{2+}, to occupy this site, whereas in PBNO-La the larger La^{3+} cation tends to induce an increased occupation of larger Pb^{2+} ions in the perovskite layer. The crystal structures reflecting the occupation of each cation in the Bi_2O_2 and perovskite layers are shown in Fig. 2(b). According to the determined occupations listed in Table 1, the chemical formulae of the three compounds are perhaps more usefully written as $(Bi_{1.88}Pb_{0.12})O_2$ $(Pb_{0.88}Bi_{0.12})Nb_2O_7$ for PBNO, $(Bi_{1.4}Pb_{0.6})O_2$ $(La_{0.5}Pb_{0.4}Bi_{0.1})Nb_2O_7$ for PBNO-La and $(Bi_{1.35}Pb_{0.65})O_2$ $(Nd_{0.5}Pb_{0.35}Bi_{0.15})Nb_2O_7$ for PBNO-Nd.

The refined unit cell parameters are given in Table 2. The unit cell volume increases for PBNO-La and decreases for PBNO-Nd. This can be attributed to the larger ionic radius of La^{3+} (1.36 Å) and smaller ionic radius of Nd^{3+} (1.27 Å) compared to Bi^{3+} (1.31 Å) for 12-fold coordination [25,26]. As compared to pristine PBNO, the substitution of La^{3+} results in a significant increase of the b and c lattice parameters, whereas the substitution of Nd^{3+} significantly decreases the a and c lattice parameters. These changes imply a decrease in the degree of orthorhombic distortion in the ab-plane with Ln^{3+} substitution, by which the a and b lattice parameters approach each other [27,28]. The decreased degree of distortion can also be expressed in terms of the orthorhombicity ratio ($(a-b)/(a+b)$) in Table 2.

We now focus on the atomic displacements in the BO_6 octahedra of the perovskite layer since these are strongly correlated to the structural distortion and break inversion symmetry, giving rise to ferroelectricity. Selected bond angles and bond distances associated with the BO_6 octahedra are summarized in Table 3. The Nb(1) cation is displaced from the center of the octahedron along the a-axis as well as along both the b- and c- axes, resulting in different Nb-O bond distances. In addition, the shortest Nb-O bond and the average Nb–O distance increase for PBNO-La and decrease for PBNO-Nd compared to PBNO. This is consistent with our conclusion that the Ln^{3+} occupy the $A(1)$-site in the perovskite layer, thus the changes in bond distances are related to the ionic radii of the Ln^{3+} ions.

The overall structural distortion also involves the tilting of the BO_6 octahedra, which is evidenced by the smaller than 180° bond angles listed in Table 3 and also visually depicted in Fig. 3. Octahedral tilting in Aurivillius phases with space group $A2_1am$ takes place around all three axes and was discussed by Aleksandrov and Bartolomé [29]; it involves a superposition of the tilt systems ($\varphi\varphi 0$) ($\varphi\varphi 0$) and ($00\psi_z$) ($00\psi_z$), where φ refers to out-of-phase tilting along the a- and b-axes of the parent $I4/mmm$ tetragonal structure, and ψ_z to in-phase tilting along the c-axis. It is therefore difficult to define an overall degree of tilting between our three samples, and we approximate the tilting by two

Table 3
Selected bond distances and bond angles associated with the BO_6 octahedra.

Bond	Bond distance (Å)		
	PBNO	PBNO-La	PBNO-Nd
Nb(1) –O(1)	2.2059(1)	2.2148(2)	2.1863(1)
Nb(1)–O(2)	1.8247(1)	1.8571(7)	1.7972(1)
Nb(1)–O(4_1)	2.1153(3)	1.9236(3)	2.0064(1)
Nb(1)–O(4_2)	1.9839(1)	1.8974(1)	1.7791(1)
Nb(1)–O(5_1)	1.8569(2)	2.1223(1)	1.9349(3)
Nb(1)–O(5_2)	1.9763(2)	2.0415(2)	2.1732(2)
Nb(1)–O average	1.993(8)	2.009(4)	1.979(4)
Bond	**Bond Angle (°)**		
	PBNO	PBNO-La	PBNO-Nd
O(2)–Nb(1) O(1)	168.17(1)	176.79(1)	169.7(3)
O(4_1)–Nb(1)–O(5_1)	159.23(2)	163.16(3)	159.35(3)
O(4_2)–Nb(1)–O(5_2)	149.27(1)	158.42(3)	158.70(5)
Nb(1)–O(1)–Nb(1)	158.64(3)	171.67(2)	164.69(2)
Nb(1)–O(4)–Nb(1)	152.64(3)	157.02(5)	150.68(1)
Nb(1)–O(5)–Nb(1)	159.89(4)	161.52(1)	169.72(2)
BO_6 tilting along c-axis	10.68	4.17	7.66
BO_6 rotation around c-axis	11.87	10.35	9.9

parameters: tilting around the a-axis as quantified by the Nb–O(1)–Nb bond angle [30,31] (Fig. 3a), and tilting in the ab-plane as defined by the relative rotation angle between neighboring octahedra around the c-axis [18] (Fig. 3b). The BO_6 octahedra are considerably tilted around the a-axis by 10.68° in PBNO, as evidenced by the Nb(1)–O(1)–Nb(1) bond angle of 158.64(3)° in Fig. 3(a). The Ln^{3+} substitution causes a substantial decrease of this tilt angle; for PBNO-La and PBNO-Nd it is 4.17° [Nb(1)–O(1)–Nb(1) bond angle: 171.67(2)°] and 7.66° [Nb(1)–O(1)–Nb (1) bond angle: 164.68(2)°], respectively. The decreased degree of tilting implies reduced structural distortion, leading to closer values of the a and b lattice parameters and a decreased orthorhombicity ratio [28]. Additionally, there is also a slight reduction of the rotation angle of BO_6 octahedra around the c-axis with Ln substitution as observed in Fig. 3(b).

In the double-layer Aurivillius phases with $A2_1am$ symmetry, the atomic displacements along the a-axis are uncompensated and give rise to an electrical dipole moment. The atomic displacements along the b- and c-axes cancel out due to the presence of glide and mirror planes [18]. The atomic displacements along the a-axis with respect to the corresponding positions in centrosymmetric tetragonal symmetry ($I4/mmm$) can be calculated from the refined atomic coordinates (Table 1), from which the total polarization (P_s) can be determined using Shimakawa's formulation [32]:

$$P_s = \sum_i \frac{m_i \times \Delta x_i \times Q_i e}{V}$$

Here m_i is the site multiplicity, Δx_i is the atomic displacement of atom i along the a-axis, $Q_i e$ is the ionic charge for the ith constituent ion, and V is the unit cell volume. The total P_s is calculated from the contributions of both the perovskite layers and Bi_2O_2 layers, by setting the position of the $A(1)$-site atom at the origin. The contribution of each ion to the total P_s is shown in Fig. 4. It is apparent that the calculated P_s decreases with Ln substitution; the values are 27.3, 15.9, and 17.2 μC/cm^2 respectively for PBNO, PBNO-La, and PBNO-Nd.

We note that the trend in P_s is also consistent with the decreased orthorhombicity and smaller octahedral tilt angles. Therefore, in our current samples, the two types of distortion associated with the atomic shifts and the octahedral tilts are likely related to each other. It has been established that the distortions are strongly affected by the stereochemically active $6s^2$ lone pair electrons of Bi^{3+}, which may favor an increase of P_s [8]. Consequently, the partial occupation of Ln^{3+} ions with no lone-pair electrons in the $A(1)$-site perovskite layers decreases both the tilting angle of the BO_6 octahedra and the

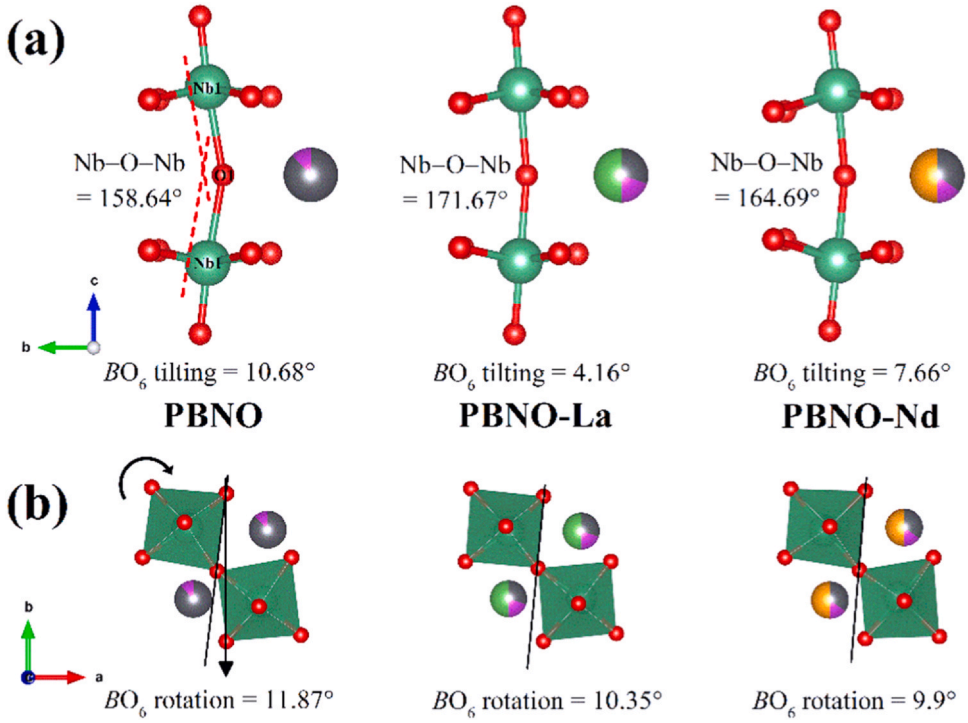

Fig. 3. Crystal structures determined from NPD data. (a) Tilting of linked BO_6 octahedra from the *c*-axis. (b) Distortion of perovskite structure projected along the *c*-axis.

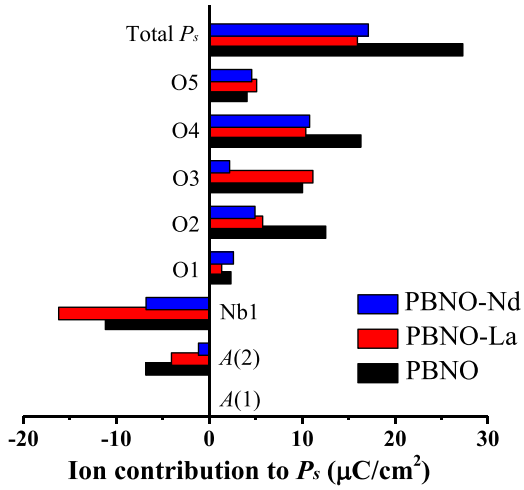

Fig. 4. Contribution to the total spontaneous polarization (P_s) of each ion determined from the atomic displacements along the *a*-axis.

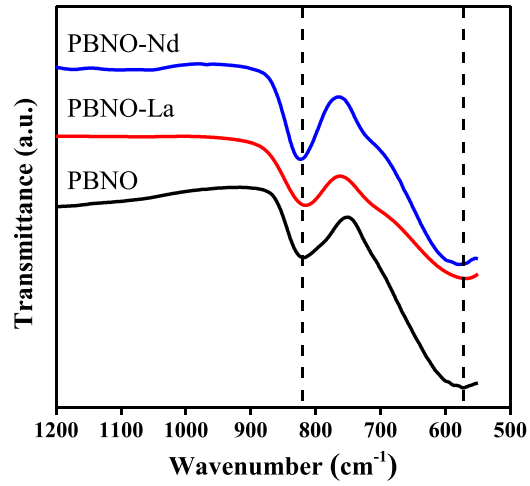

Fig. 5. FTIR spectra of samples at room temperature.

atomic displacements. Moreover, the smaller ionic radius of Nd^{3+} compared to La^{3+} induces a greater degree of distortion, suggesting that the substitution of smaller cations could be more effective regarding the electrical properties [33].

The changes in local structure were investigated using FTIR spectroscopy at room temperature in the range 550–1200 cm^{-1}, corresponding to the internal modes of the BO_6 octahedra (> 200 cm^{-1}). The FTIR spectra in Fig. 5 show two vibration modes of PBNO at 573 and 820 cm^{-1} with assignments of asymmetric *B*–O stretching and symmetric *B*–O stretching of the BO_6 octahedra, respectively [34]. Both vibration modes of BO_6 should not change, since the Ln^{3+} ions do not substitute into the *B*-site of the perovskite layers. However, a slight shifting is observed in both modes as shown in Fig. 5, which is induced by the occupation of Ln^{3+} on the *A*-site of the perovskite layer [19,20], as revealed by neutron diffraction analysis. The substitution of larger La^{3+} results in a longer Nb–O bond and thereby lowered bond strength, shifting the vibration modes to lower wavenumbers of 565 and 813 cm^{-1}. Conversely, the substitution of smaller Nd^{3+} results in shifts toward higher wavenumbers of 579 and 826 cm^{-1}, since the Nb-O bond is shorter and results in higher bond strength [21]. We note that the IR spectra do not show sulfate vibration modes around 970–995 cm^{-1}, which indicates that the salts used as the reaction media do not react with the products.

SEM micrographs of the powder samples are shown in Fig. 6. It is observed that the grain growth is highly anisotropic with plate-like grain morphologies, which is a characteristic feature of bismuth layer-structured compounds. The grain size of PBNO is in the range 1.08–1.97 μm and is reduced in size with Ln^{3+} substitution, to the range 0.55–0.88 μm for PBNO-La and 0.72–1.24 μm for PBNO-Nd. The Ln^{3+} ions are known to suppress grain growth, which is attributed to their low diffusivity [17]. In contrast, Bi^{3+} is reported to have high ionic mobility and can stimulate grain growth, thus grain growth will be inhibited with reduced Bi^{3+} content.

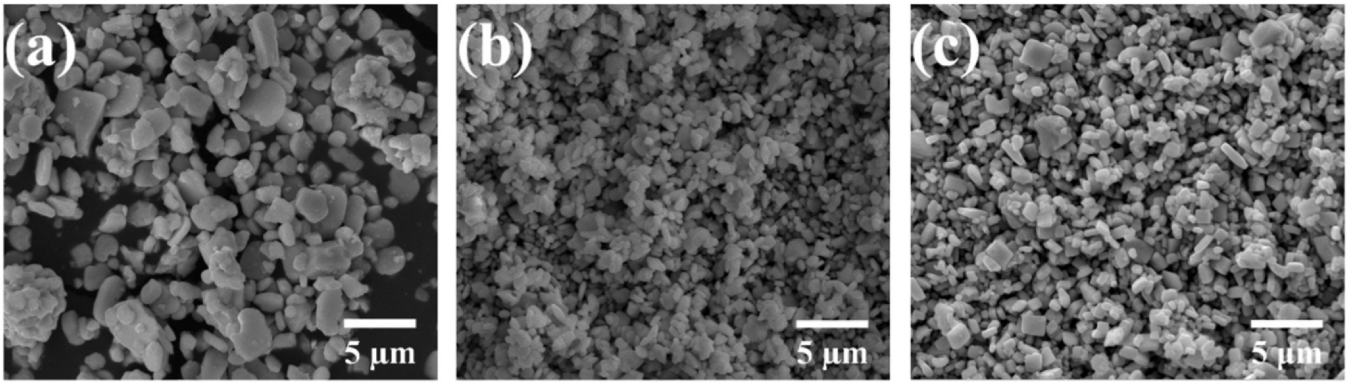

Fig. 6. SEM micrographs of the powder samples. (a) PBNO, (b) PBNO-La, (c) PBNO-Nd.

Fig. 7 shows the temperature dependence of the dielectric constant and dielectric loss of pelletized samples measured in the range 50 kHz to 1 MHz, which best reflects the intrinsic polarizability [35]. The density of the pellets was determined as 7.73 g/cm^3, 7.57 g/cm^3, and 7.64 g/cm^3 for PBNO, PBNO-La, and PBNO-Nd respectively, which in each case is greater than 93% of the theoretical density and indicates that the molten salt method produces dense grains [21]. A single dielectric peak is observed for all the samples, which corresponds to the phase transition from the ferroelectric to paraelectric phase (T_c). The T_c decreases from 828 K for PBNO to 508 K for PBNO-La and 613 K for PBNO-Nd. The decrease in T_c with Ln^{3+} substitution is consistent with the reduction in the degree of octahedral tilting and calculated P_s value, as discussed in the neutron diffraction analysis above. In addition, the T_c of PBNO-Nd is higher than that of

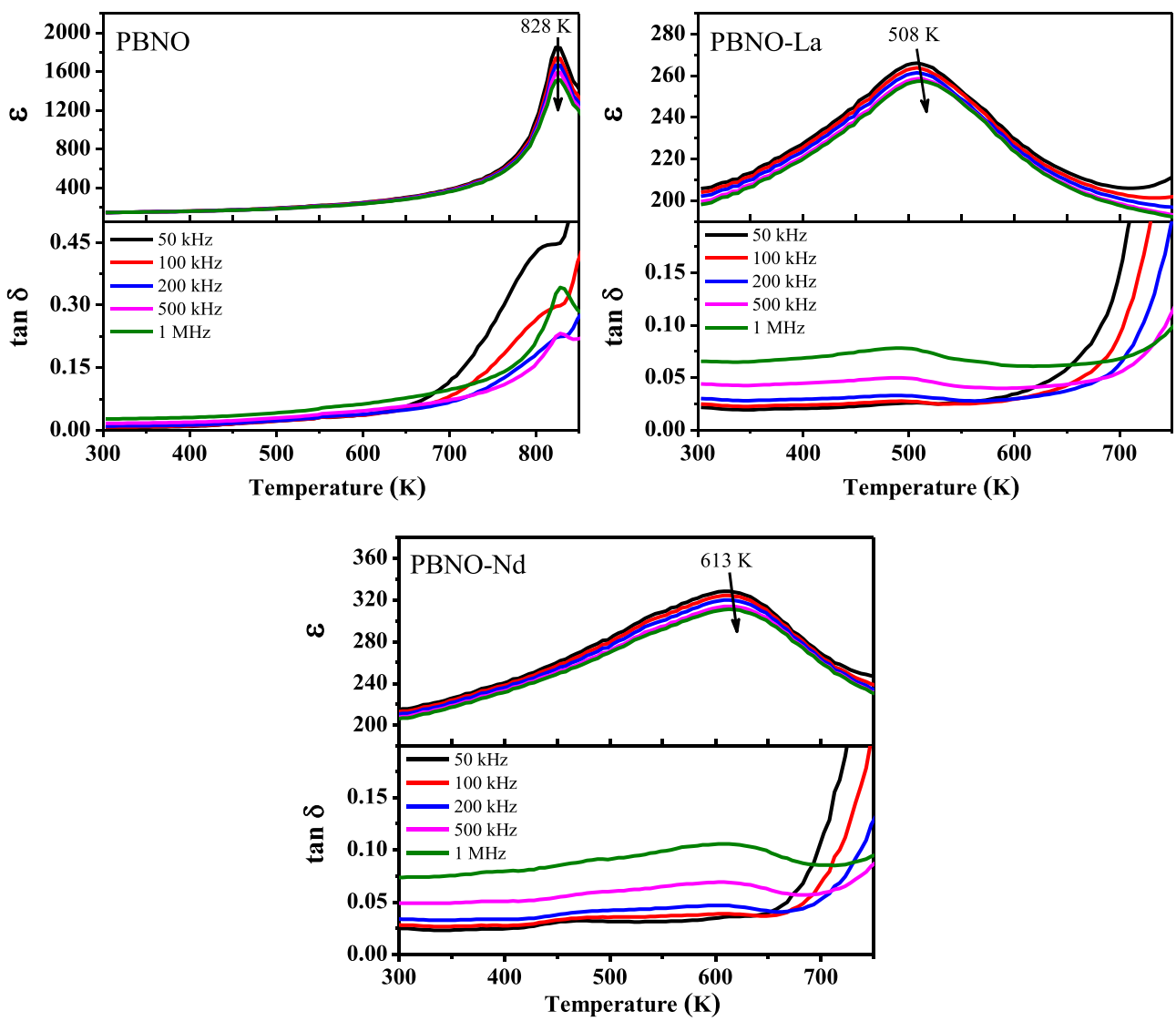

Fig. 7. Variation of dielectric constant (ε) and dielectric loss (tan δ) as a function of temperature and at different frequencies.

Table 4
Variation of electrical properties of samples measured at 1 MHz.

Sample	ε_{RT}	T_c (K)	ε_m	tan δ (T_m)	(a-b)/ (a+b)	γ	ΔT (K)
PBNO	146	828	1740	0.297	0.00145	1.27	0
PBNO-La	198	508	257	0.077	0.00019	1.63	5
PBNO-Nd	206	613	324	0.039	0.00024	1.65	5

PBNO-La as the ionic radius of Nd^{3+} is smaller than La^{3+}, and T_c is known to increase with decreasing *A*-site ionic radius [31].

At T_c a significant decrease in dielectric constant (ε_m) and dielectric loss (tan δ) is observed with Ln^{3+} substitution, as shown in Table 4. The magnitude of ε_m is correlated to the grain size; decreasing grain size inhibits the movement of domain walls, contributing to the decrease in magnitude. The significant reduction of dielectric loss with Ln^{3+} substitution is attributed to the suppression of intrinsic oxygen vacancies that are created due to bismuth volatilization at high temperatures [8,9]. We also suggest that the trend in dielectric loss is also consistent with the trend in grain size. Smaller grains with more grain boundaries will tend to inhibit charge transport, resulting in lower dielectric loss [36,37].

Relaxor-ferroelectric behavior is initially observed in the PBNO-La and PBNO-Nd samples and is characterized by the broadened phase transition peaks and the frequency-dispersive behavior in Fig. 7(b) and (c) [6]. The dielectric peaks of both samples in the frequency range 50 kHz to 1 MHz shift slightly by ~5 K (ΔT), which can be attributed to the contribution of ferroelectric nano-domain motion. This relaxor behavior can also be evaluated by the degree of diffuseness (γ) calculated from the modified Curie-Weiss law equation [11]:

$$\frac{1}{\varepsilon_r} - \frac{1}{\varepsilon_m} = \frac{(T - T_m)^\gamma}{C}$$

Here ε_m is the dielectric maximum at the transition temperature T_m, C is a Curie-type constant, and γ is the degree of diffuseness. A normal ferroelectric is known to follow $\gamma = 1$, whereas for a relaxor the behavior follows $\gamma = 2$. The γ value is fitted from plots of $\ln(1/\varepsilon_r - 1/\varepsilon_m)$ versus $\ln(T\text{-}T_m)$ in Fig. 8. The increased γ values for PBNO-La and PBNO-Nd indicate a changeover from normal ferroelectric to relaxor behavior, which leads to an increase in ΔT as listed in Table 4. This is induced by the increased disorder of the *A*-site cations (Pb/Bi/La or Nd) in the perovskite layer as well as the disordered *A*-site cations (Pb/Bi) in the Bi_2O_2 layer, as explained in the neutron

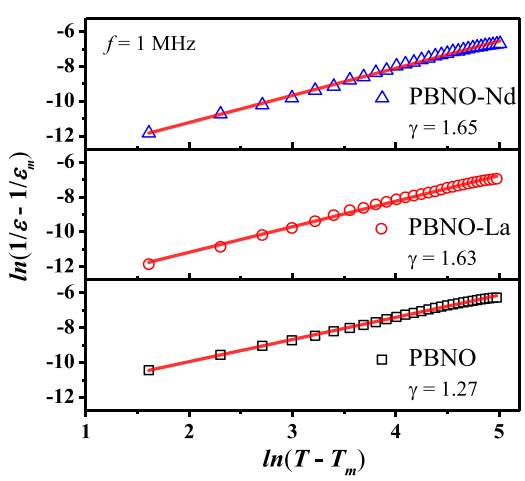

Fig. 8. Modified Curie-Weiss fitted lines to quantify the relaxor ferroelectric behavior.

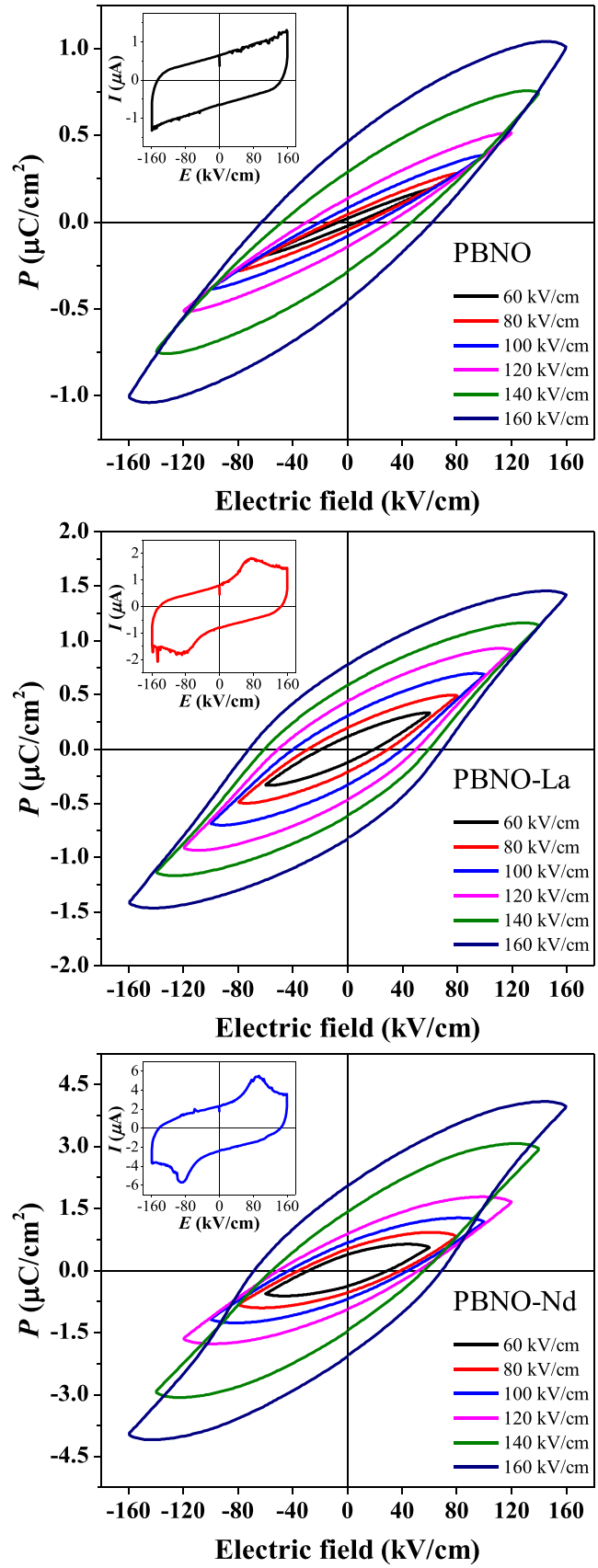

Fig. 9. *P-E* hysteresis loops measured at room temperature and 1 Hz frequency.

diffraction analysis above. The disorder leads to the breaking of long-range ferroelectric order into polar nanoregions, which is manifested by relaxor behavior.

Since all three samples show a peak in the dielectric constant suggesting the onset of ferroelectricity, polarization-electric field (*P-E*) hysteresis loops were performed at room temperature at a frequency of 1 Hz, as shown in Fig. 9. The *P-E* loops are unsaturated, implying that the domains are not fully aligned at the highest electric fields of 160 kV/cm. Although unsaturated, all three samples exhibit ferroelectric behavior, as indicated by the increase of both the remnant polarization (P_r) and saturated polarization (P_s) in non-linear fashion as the electric field increases [23,38].

The *P-E* loop of pristine PBNO suggests that this sample exhibits capacitor behavior rather than ferroelectric behavior, as there is no obvious switching peak in the *I-E* curve (inset to Fig. 8a). For the PBNO-La and PBNO-Nd samples, the *P-E* hysteresis loops are accompanied by ferroelectric domain switching, as apparent in the insets to Fig. 9(b) and (c), indicating improved ferroelectric properties. These phenomena initially appear to be in conflict with the decreased values of P_s calculated from the structural distortion, as discussed above. We assume that the ferroelectric domains of pristine PBNO are frozen and cannot be reoriented in the external fields applied, since the measurement was performed at RT (300 K), well below the high T_c (828 K), whereas the T_c of PBNO-La (508 K) and PBNO-Nd (603 K) are closer to the measurement temperature, making it easier to align the ferroelectric domains in these two samples. It has been reported that the switching polarization increases with increasing temperature and electric field [39]. A tendency towards well-saturated *P-E* loops was observed previously for the double-layer Aurivillius phase $Sr_{1-x}(K_{0.5}Bi_{0.5})_xBi_2Nb_2O_9$, where a higher measurement temperature of 180 ºC was used [40]. Thus, we suggest that the P_s and P_r of the PBNO sample will increase and show a well-defined loop at elevated temperatures, as well as exhibiting a higher dielectric constant with increasing temperature as shown in Fig. 7. We also assume that the lower measured P_s values for all three samples compared to the calculated values is due to the unsaturated polarization in the room temperature measurements.

Due to the easier alignment of the ferroelectric domains, the P_r increases to 0.79 μC/cm^2 for PBNO-La and 2.06 μC/cm^2 for PBNO-Nd as compared to 0.47 μC/cm^2 for pristine PBNO at an applied field of 160 kV/cm. This trend is consistent with the magnitude of the room-temperature dielectric constant (ε_{RT}), listed in Table 4. The higher P_r values and ε_{RT} are attributed to the reduction of oxygen vacancies as well as dielectric loss, since charge transport is inhibited in the *Ln*-substituted materials [36].

4. Conclusions

The double-layer Aurivillius phase $PbBi_2Nb_2O_9$ was prepared by the molten-salt method with partial substitution of lanthanide ions (*Ln*: La^{3+}, Nd^{3+}) for Bi^{3+} ions. X-ray diffraction confirmed that all the samples are single-phase and adopt non-centrosymmetric orthorhombic $A2_1am$ symmetry. The Ln^{3+} ions inhibit grain growth, reducing the size of the grains with plate-like morphology. Neutron diffraction data indicated that the Ln^{3+} ions occupy the *A*-site of the perovskite layer and that Pb^{2+} and Bi^{3+} ions occupy the *A*-site of both the perovskite and Bi_2O_2 layers. With Ln^{3+} substitution, the degree of orthorhombicity decreases and the BO_6 octahedral distortion decreases, which are related to the decreased ferroelectric transition temperatures (T_c). This is also consistent with a decrease in the overall ferroelectric distortion as the effect of the $6s^2$ lone pair electrons of Bi^{3+} is diminished. Relaxor-ferroelectric behavior is induced with Ln^{3+} substitution since the degree of disorder of the *A*-site cations on both the perovskite and Bi_2O_2 layers increases. The remnant polarization (P_r) at room temperature is significantly increased for PBNO-Nd and PBNO-La, which is attributed to the higher dielectric constant at room temperature and decreased dielectric loss.

CRediT authorship contribution statement

Tio P. Wendari: Investigation, Methodology, Visualization, Writing - original draft. **Syukri Arief:** Conceptualization, Writing - review & editing. **Nandang Mufti:** Conceptualization, Validation. **Andon Insani:** Resources, Methodology. **Jacob Baas:** Investigation, Formal analysis. **Graeme R. Blake:** Resources**,** Validation, Writing - review & editing. **Zulhadjri:** Supervision, Conceptualization, Validation, and Writing - original draft.

Declaration of Competing Interest

The authors declare that they have no known competing financial interests or personal relationships that could have appeared to influence the work reported in this paper.

Acknowledgments

The authors gratefully acknowledge financial support from the Ministry of Research, Technology and Higher Education (RISTEKDIKTI) of the Republic of Indonesia through the PMDSU Scholarship [Grant number 050/SP2H/LT/DRPM/2018] and the PKPI-PMDSU Scholarship [Grant number 1406.29/D3/PG/2018].

References

[1] J.F. Scott, Ferroelectric Memories, 1st ed.,, Springer-Verlag Berlin Heidelberg,, New York, 2000, https://doi.org/10.1007/978-3-662-04307-3
[2] N. Setter, R. Waser, Electroceramic materials, Acta Mater. 48 (2000) 151–178, https://doi.org/10.1016/S1359-6454(99)00293-1
[3] S. Zhang, F. Yu, Piezoelectric materials for high temperature sensors, J. Am. Ceram. Soc. 94 (2011) 3153–3170, https://doi.org/10.1111/j.1551-2916.2011.04792.x
[4] W. Gao, Y. Zhu, Y. Wang, G. Yuan, J.M. Liu, A review of flexible perovskite oxide ferroelectric films and their application, J. Mater. 6 (2020) 1–16, https://doi.org/10.1016/j.jmat.2019.11.001
[5] B. Aurivillius, Mixed bismuth oxides with layer lattices 1. The structure type of $CaNb_2Bi_2O_9$, Ark För Kemi 1 (1949) 463–480.
[6] H. Du, Y. Li, H. Li, X. Shi, C. Liu, Relaxor behavior of bismuth layer-structured ferroelectric ceramic with *m* = 2, Solid State Commun. 148 (2008) 357–360, https://doi.org/10.1016/j.ssc.2008.05.017
[7] B. Yang, M. Guo, X. Tang, R. Wei, L. Hu, J. Yang, W. Song, J. Dai, X. Lou, X. Zhu, Y. Sun, Lead-free $A_2Bi_4Ti_5O_{18}$ thin film capacitors (*A* = Ba and Sr) with large energy storage density, high efficiency, and excellent thermal stability, J. Mater. Chem. C 7 (2019) 1888–1895, https://doi.org/10.1039/c8tc05558k
[8] Q. Chang, H. Fan, C. Long, Effect of isovalent lanthanide cations compensation for volatilized *A*-site bismuth in aurivillius ferroelectric bismuth titanate, J. Mater. Sci. Mater. Electron. 28 (2017) 4637–4646, https://doi.org/10.1007/s10854-016-6102-0
[9] A. Khokhar, P.K. Goyal, O.P. Thakur, A.K. Shukla, K. Sreenivas, Influence of lanthanum distribution on dielectric and ferroelectric properties of $BaBi_{4-x}La_xTi_4O_{15}$ ceramics, Mater. Chem. Phys. 152 (2015) 13–25, https://doi.org/10.1016/j.matchemphys.2014.11.074
[10] P. Nayak, T. Badapanda, S. Panigrahi, Thermal stability and improved electrical properties in $Sr_{1-x}Gd_{2x/3}Bi_4Ti_4O_{15}$ ceramics, Mater. Lett. 204 (2017) 120–124, https://doi.org/10.1016/j.matlet.2017.06.025
[11] A. Axelsson, F. Le Goupil, M. Valant, N.M. Alford, Electrocaloric effect in lead-free aurivillius relaxor ferroelectric ceramics, Acta Mater. 124 (2017) 120–126, https://doi.org/10.1016/j.actamat.2016.11.001
[12] L. Sun, C. Feng, L. Chen, S. Huang, Dielectric and piezoelectric properties of $SrBi_{2-x}Sm_xNb_2O_9$ (x = 0, 0.05, 0.1, 0.2, 0.3, and 0.4) ceramics, J. Am. Ceram. Soc. 90 (2007) 3875–3881, https://doi.org/10.1111/j.1551-2916.2007.02064.x
[13] M. Verma, K. Sreenivas, V. Gupta, Influence of La doping on structural and dielectric properties of $SrBi_2Nb_2O_9$ ceramics, J. Appl. Phys. 105 (2009) 024511, https://doi.org/10.1063/1.3068368
[14] L. Sun, C. Feng, L. Chen, S. Huang, Dielectric relaxation in layer-structured $SrBi_{2-x}Nd_xNb_2O_9$ ceramics (x = 0, 0.05, 0.2, 0.35), J. Am. Ceram. Soc. 90 (2007) 322–326, https://doi.org/10.1111/j.1551-2916.2006.01405.x
[15] S.-J. Oh, Y. Shin, T.T. Tran, D.W. Lee, A. Yoon, P.S. Halasyamani, K.M. Ok, Structure-property relationships in solid solutions of noncentrosymmetric aurivillius phases, $Bi_{4-x}La_xTi_3O_{12}$ (x = 0 − 0.75), Inorg. Chem. 51 (2012) 10402–10407, https://doi.org/10.1021/ic301615f
[16] B.A. Hunter, Rietica - A Visual Rietveld Program, Australian Nuclear Science and Technology Organisation,, Australia, 2000.

[17] Z. Peng, X. Zeng, F. Cao, X. Yang, Microstructure and impedance properties of La, Ce multi-rare earth ions doped $Na_{0.5}Bi_{2.5}Nb_2O_9$ aurivillius type ceramics, J. Alloy. Compd. 695 (2017) 626–631, https://doi.org/10.1016/j.jallcom.2016.11.127
[18] G. Liu, S. Ren, C. Wu, D. Wang, F. Li, J. Wu, Q. Chen, Enhanced thermal stability of (NaCe)-multidoped $CaBi_2Nb_2O_9$ by *A*-site vacancies-induced pseudo-tetragonal distortion, J. Am. Ceram. Soc. 101 (2018) 4615–4626, https://doi.org/10.1111/jace.15724
[19] V. Koval, I. Skorvanek, G. Viola, M. Zhang, C. Jia, H. Yan, Crystal chemistry and magnetic properties of Gd-Substituted aurivillius-type $Bi_5FeTi_3O_{15}$ ceramics, J. Phys. Chem. C 122 (2018) 15733–15743, https://doi.org/10.1021/acs.jpcc.8b03801
[20] X. Xie, Z. Zhou, T. Chen, R. Liang, X. Dong, Enhanced electrical properties of NaBi modified $CaBi_2Nb_2O_9$-based aurivillius piezoceramics via structural distortion, Ceram. Int. 45 (2019) 5425–5430, https://doi.org/10.1016/j.ceramint.2018.11.244
[21] Zulhadjri, T.P. Wendari, U. Septiani, S. Arief, Investigation on structure, dielectric and magnetic properties of the four-layer aurivillius phase Pb1-$Bi_{3.5}$+$Nd_{0.5}Ti_4$-MnO_{15} prepared via molten salt method, J. Solid State Chem. 292 (2020) 121723, https://doi.org/10.1016/j.jssc.2020.121723
[22] J. Zhu, X.B. Chen, Z.P. Zhang, J.C. Shen, Raman and X-ray photoelectron scattering study of lanthanum-doped strontium bismuth titanate, Acta Mater. 53 (2005) 3155–3162, https://doi.org/10.1016/j.actamat.2005.03.020
[23] T.P. Wendari, S. Arief, N. Mufti, A. Insani, J. Baas, G.R. Blake, Zulhadjri, Structural and multiferroic properties in double-layer aurivillius phase $Pb_{0.4}Bi_{2.1}La_{0.5}Nb_{1.7}Mn_{0.3}O_9$ prepared by molten salt method, J. Alloy. Compd. 820 (2020) 153145, https://doi.org/10.1016/j.jallcom.2019.153145
[24] Ismunandar, B.A. Hunter, B.J. Kennedy, Cation disorder in the ferroelectric aurivillius phase $PbBi_2Nb_2O_9$: an anamolous dispersion X-ray diffraction study, Solid State Ion. 112 (1998) 281–289, https://doi.org/10.1016/S0167-2738(98)00222-7
[25] R.D. Shannon, Revised effective ionic radii and systematic studies of interatomic distances in halides and chalcogenides, Acta Crystallogr. Sect. A 32 (1976) 751–767.
[26] J. Tellier, P. Boullay, M. Manier, D. Mercurio, A comparative study of the aurivillius phase ferroelectrics $CaBi_4Ti_4O_{15}$ and $BaBi_4Ti_4O_{15}$, J. Solid State Chem. 177 (2004) 1829–1837, https://doi.org/10.1016/j.jssc.2004.01.008
[27] E.V. Ramana, N.V. Prasad, D.M. Tobaldi, J. Zavašnik, M.K. Singh, M.J. Hortigüela, M.P. Seabra, G. Prasad, M.A. Valente, Effect of samarium and vanadium co-doping on structure, ferroelectric and photocatalytic properties of bismuth titanate, RSC Adv. 7 (2017) 9680–9692, https://doi.org/10.1039/c7ra00021a
[28] A.B. Missyul, I.A. Zvereva, T.T.M. Palstra, A.I. Kurbakov, Double-layered aurivillius-type ferroelectrics with magnetic moments, Mater. Res. Bull. 45 (2010) 546–550, https://doi.org/10.1016/j.materresbull.2010.02.002
[29] K.S. Aleksandrov, J. Bartolomé, Structural distortions in families of perovskite-like crystals, Phase Transit. 77 (2001) 255–335, https://doi.org/10.1080/01411590108228754
[30] J. Yuan, R. Nie, W. Li, J. Zhu, Impact of crystal structure and defect on the electric properties in (LiCeY)-doped $CaBi_2Nb_2O_9$-based high-temperature piezoceramics, J. Mater. Sci. Mater. Electron. 30 (2019) 5240–5248, https://doi.org/10.1007/s10854-019-00823-1
[31] C. Long, H.F. Fan, P. Ren, Structure, phase transition behaviors and electrical properties of Nd substituted aurivillius polycrystallines $Na_{0.5}NdxBi_{2.5}$–xNb_2O_9 (x = 0.1, 0.2, 0.3, and 0.5), Inorg. Chem. 52 (2013) 5045–5054, https://doi.org/10.1021/ic302769h
[32] Y. Shimakawa, Y. Kubo, Y. Tauchi, T. Kamiyama, H. Asano, F. Izumi, Structural distortion and ferroelectric properties of $SrBi_2(Ta_{1-x}Nb_x)_2O_9$, Appl. Phys. Lett. 77 (2000) 2749–2751, https://doi.org/10.1063/1.1319509
[33] C. Long, Q. Chang, Y. Wu, W. He, Y. Li, H. Fan, New layer-structured ferroelectric polycrystallines, $Na_{0.5}NdxBi_{4.5}$-xTi_4O_{15}: crystal structures, electrical properties and conduction behaviors, J. Mater. Chem. C 3 (2015) 8852–8864, https://doi.org/10.1039/b000000x
[34] V.D. Phadtare, V.R. Puri, Studies on electrical and dielectric properties of co-precipitated aurivillius phase $Ca_{1-x}Ba_xBi_2Nb_2O_9$ ceramics, Ceram. Int. 42 (2016) 8581–8586, https://doi.org/10.1016/j.ceramint.2016.02.087
[35] Z. Zulhadjri, A.A. Billah, T.P. Wendari, E. Emriadi, A.A. Septiani, S. Arief, Synthesis of Aurivillius phase $CaBi_4Ti_4O_{15}$ doped with both La^{3+} and Mn^{3+} cations: Crystal structure and dielectric properties, Mat. Res. 23 (2020) e20190521, https://doi.org/10.1590/1980-5373-MR-2019-0521
[36] X. Li, Z. Chen, L. Sheng, L. Li, W. Bai, F. Wen, P. Zheng, W. Wu, L. Zheng, Y. Zhang, Remarkable piezoelectric activity and high electrical resistivity in Cu/Nb co-doped $Bi_4Ti_3O_{12}$ high temperature piezoelectric ceramics, J. Eur. Ceram. Soc. 39 (2019) 2050–2057, https://doi.org/10.1016/j.jeurceramsoc.2019.01.042
[37] T.P. Wendari, S. Arief, N. Mufti, J. Baas, G.R. Blake, Ratio effect of salt fluxes on structure, dielectric and magnetic properties of La,Mn-doped $PbBi_2Nb_2O_9$ Aurivillius phase, Ceram. Int. 46 (2020) 14822–14827, https://doi.org/10.1016/j.ceramint.2020.03.007
[38] M.R. Dolgos, U. Adem, A. Manjon-sanz, X. Wan, T.P. Comyn, T. Stevenson, J. Bennett, A.J. Bell, T.T. Tran, P.S. Halasyamani, J.B. Claridge, M.J. Rosseinsky, Perovskite B-Site compositional control of $[110]_p$ polar displacement coupling in an ambient-pressure-stable bismuth-based ferroelectric, Angew. Chem. 124 (2012) 10928–10933, https://doi.org/10.1002/ange.201203884
[39] R. Nie, J. Yuan, Q. Chen, J. Xing, J. Zhu, W. Zhang, Crystal distortion and electrical properties of Ce-doped BIT-based piezoelectric ceramics, J. Am. Ceram. Soc. 102 (2019) 5432–5442, https://doi.org/10.1111/jace.16421
[40] Z. Yao, R. Chu, Z. Xu, J. Hao, W. Li, G. Li, Processing and enhanced electrical properties of Sr1-x$(K_{0.5}Bi_{0.5})xBi_2Nb_2O_9$ lead-free piezoelectric ceramics, Ceram. Int. 42 (2016) 10619–10623, https://doi.org/10.1016/j.ceramint.2016.03.156